2014

Metamorphism of Cretaceous Standstones by Natural Coal-Fires, San Rafael Swell, Utah

Alexa R. Zilberfarb
Scripps College

Metamorphism of Cretaceous sandstones by natural coal-fires, San Rafael Swell, Utah

A Thesis Presented

by

Alexa R. Zilberfarb

To the Pomona College Geology Department

in partial fulfillment of

the degree of Bachelor of Arts

Senior Thesis in Geology

April 25, 2014

Advised by:

Jade Star Lackey
Primary Research Advisor

Robert Gaines
Reader

ABSTRACT

Underground coal fires commonly metamorphose or melt surrounding rocks at temperatures exceeding 1000°C. Numerous “baked” sandstone clinker deposits occur in the Cretaceous sedimentary rocks exposed in the San Rafael Swell, UT. This study examines clinker in three main localities: 1) East Carbon, UT, 2) Helper, UT, and 3) Emery, UT. The extent of pyrometamorphism in these areas is variably developed, but reached high enough temperature in Helper, UT to initiate melting and the production of paralavas. These paralavas were examined compositionally and mineralogically to determine melting conditions, peak temperatures, and mobility of different metals as a result of pyrometamorphism. X-ray diffraction and petrographic analysis showed that paralavas in the Helper locality contain the high temperature SiO_2 polymorphs tridymite and cristobalite which alone indicate temperatures exceeding 875°C in several samples. Paralavas containing diopside+tridymite and cordierite+mullite+cristobalite provide more restrictive estimates of temperature as they form cotectic and eutectic assemblages in the SiO_2-Mgo-CaO and SiO_2-MgO-Al_2O_3, respectively. The assemblages indicate minimum temperatures of melting and metamorphism of 1330–1465ºC. The high temperatures of the paralavas generate increased metal mobility, potentially signifying a hazard if leached out into the environment.

TABLE OF CONTENTS

FIGURES AND TABLES

FIGURES AND TABLES (CONT.)

INTRODUCTION

Coal seams ignite through a variety of reasons; Fire may start by spontaneous combustion, lightning strikes, or human error (Masalehdani et al., 2007). Spontaneous combustion occurs because of the buildup of heat that is generated from the interaction of coal and oxygen. The oxidation of coal causes the formation of gases, predominately CO and CO_2. Combustion occurs when the ignition temperature of coal is reached (Gaweda et al., 2013). Mining or erosion often exposes coal seams, leaving them open to the elements. In addition, development of coal bed methane requires water to be drawn out of the coal to mobilize the methane, thus leaving the coal dry and prone to combustion. These coal fires produce intense heat and large-scale fires that can burn for decades, or even centuries (e.g. China) unregulated (Stracher and Taylor, 2004). Coal fires in northern China consume up to 200 millions tons of coal per year, and account for 2–3% of the yearly world emission of atmospheric CO_2 from burning fossil fuels (Stracher and Taylor, 2004). These fires can reach temperatures higher than 1000ºC, and this extreme heat over long periods of time will metamorphose the host rock.

Metals such as lead, mercury, and copper pose health risks when they are mobilized and could leach into the groundwater. These metals can cause severe kidney damage and circulatory problems if ingested. The EPA lists the maximum contamination limit (MCL) of lead in water at 15 ppb, and copper 1.3 ppm (U.S.EPA, 2012). Coal mining releases metals into the environment when coals are combusted in power plants through fly ash (Meji and te Winkel, 2007). These heavy metals will leach to the location where coal is being mined, but can be minimized through abatement procedures.

When sedimentary deposits are burned from coal fires, the material surrrounding the coal seam is pyrometamorphosed, sometimes resulting in a paralava (Masalehdani et al., 2007). Paralava is defined as a low-grade metamorphic rock that is formed adjacent to coal seams. This type of rock is highly vesicular and often mistaken for basalt (Grapes, 2006). Pyrometamorphism occurs at high temperatures (>1000ºC) and low pressure (≤1 kbar) (Cosca et al., 1989). However, there has not been extensive quantitative (i.e. temperature, rate of burning) research done on such deposits (Cosca et al., 1989).

This study of the pyrometamorphosed sandstones in southeast Utah explores changes in mineralogical and chemical composition that result from natural coal fires. The intersection of research between coal fire and metal mobility has the potential to discover ways of mitigating metal mobility through looking at pyrometamorphosed deposits. Once released, these metals such as Pb, Co, Cu persist in the environment (Smith, 2007). Fires will make metals more mobile, and the analyses of unaltered vs. pyrometamorphosed material are used to test this hypothesis.

Background

For coal fires to continue burning, the coal needs both oxygen and an escape vent for the release of smoke, vapor, and gas. Chimneys form as fissures because of subsidence as the coal is burned away and the underlying layer decreases in volume (Heffern and Coates, 2004). These chimneys act as this two-way exchange between the underground coal seam and the surface. Figure 1 depicts a typical "clinker geomorphology". Clinker deposits are defined as a low-grade metamorphic rock that has been baked or partially melted because of pyrometamorphism (Grapes, 2006). Cosca et al. (1989), explained in detail typical minerals found in paralava and clinker deposits through the study of the Powder River Basin, Wyoming. Rapid cooling of the melt may be caused by abrupt fractures to the surface as chimneys form, allowing for the permeation of cooler air into the system, and thus allowing minerals to be quenched directly from the liquid. Cosca et al. (1989) highlighted characteristic minerals found in clinker and paralava deposits: (1) Clinopyroxene, a common mineral in paralavas, which ranges in composition from diopside ($CaMgSi_2O_6$) to esseneite ($CaFe^{3+}[AlSiO_6]$); (2) Orthopyroxene occurs as fine needles, though is rare; 3) Fayalite olivine (Fe_2SiO_4) occurs as subhedral skeletal grains; (4) Quartz, tridymite, and cristobalite (all SiO_2) can be found in paralava, but usually only one polymorph is seen; (5) Anorthite ($CaAl_2Si_2O_8$) is the most profuse feldspar, though (6) spinel ($MgAl_2O_4$) is also common in paralava. Cosca et al. (1989), also notes that the most striking composition difference between clinker and paralava is the concentration of Fe, as Fe is enriched in the paralava. This enrichment could possibly be caused by increased heat allowing for metal mobility. Clinker deposits have thus been located by their magnetic anomalies (Lindqvist et al., 1983).

Lewis and Clark noted the distinct red color of the natural clinker deposits in Wyoming during their journey west (Bluemle, 2005). One of the first scientific explorations of clinker deposits came from Cecil Tilley's 1924 paper that examined contact metamorphism in England. At this time, clinker deposits were known as buchite, and this terminology continued into the late 1980's (Foit, et al, 1987). The parochial term of the pyrometamorphic deposits in the U.S. is "clinker", an allusion to the sound these fine-grained rocks make when broken or struck.

Combustion metamorphism has occurred in a variety of regions, including Australia, Israel, and the Western United States from Montana to Texas (Clark, 1992). Other examples include Italy (Melluso et al., 2003; Capitiano et al., 2004), China (Stracher and Taylor, 2004; Grapes et al., 2009), and New Zealand (Masalehdani et al., 2007). Most of these areas are mining regions, and such activities expose fresh coal to oxygen in the air through mine shafts, therefore intensifying the fires when they do occur. Many parts of China are experiencing coal fires in mine areas, and are

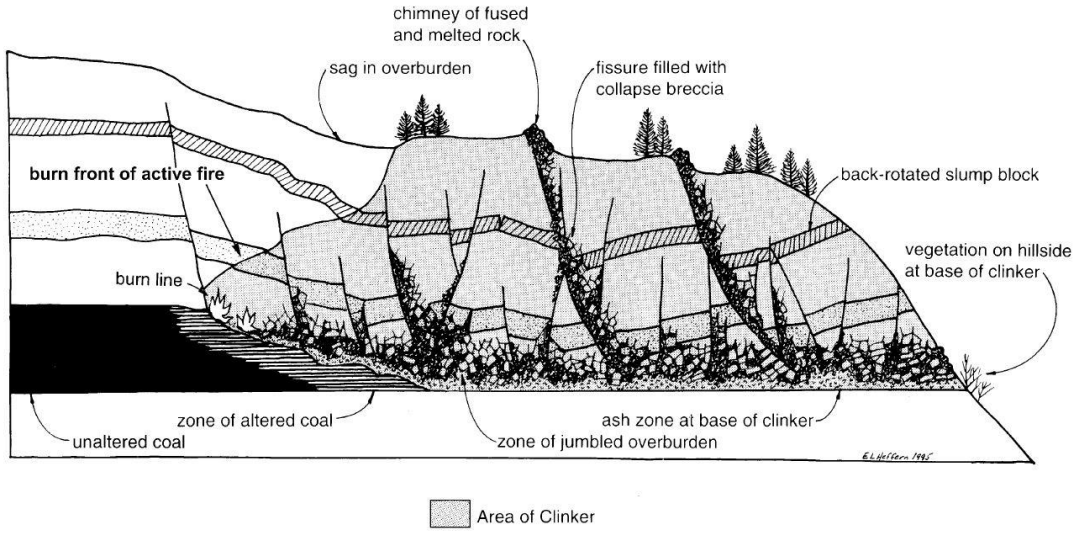

Figure 1: Cross section of typical coal fire geomorphology where transition from unburned coal to burn zone results in downward collapse of overlying strata and listric normal faulting (fissures). Fissures act as chimney structures allowing for two-way gas exchange from coal seam to surface and promote continued burning (from right to left) of the coal until the water table is encountered or oxygen levels become too low. From Heffern and Coates (2004).

thus experiencing significant health risks. China's coal fires are considered the most severe in the world (Stracher and Taylor, 2004). Active coal fires burn in the United States as well, including the study area (Stracher et al, 2005), but it was the 1962 Centralia, Pennsylvania fire that brought national public awareness to this potential hazard. The Centralia fire is considered the worst coal fire disaster in U. S. history. Burning trash ignited anthracite in a coal seam and spread to the mine beneath the town (Geissinger, 1990). The town was abandoned because of the release of toxic gases, subsidence, and polluted streams (Stracher and Taylor, 2004). The Centralia fire may burn for 100 or more years (Memmi, 2000). Pennsylvania and the Powder River Basin in Wyoming have the highest concentration of coal in the U.S., and thus the most coal fires

The geologic setting is in east central Utah, near the San Rafael Swell and the Book Cliffs in Emery and Carbon Counties (Fig. 2), and comprises of a series of Cretaceous sedimentary rocks deposited along the western margin of the Cretaceous Western Interior Seaway (Stracher et al., 2005). This seaway stretched from the Gulf of Mexico to the Arctic and covered eastern and central Utah (Stracher et al., 2005). The San Rafael Swell, an anticline formed during the Laramide orogeny, consists of deposits from the Interior Seaway and associated non-marine environments. The San Rafael Swell is part of the Colorado Plateau, an area of uplift roughly centering on the

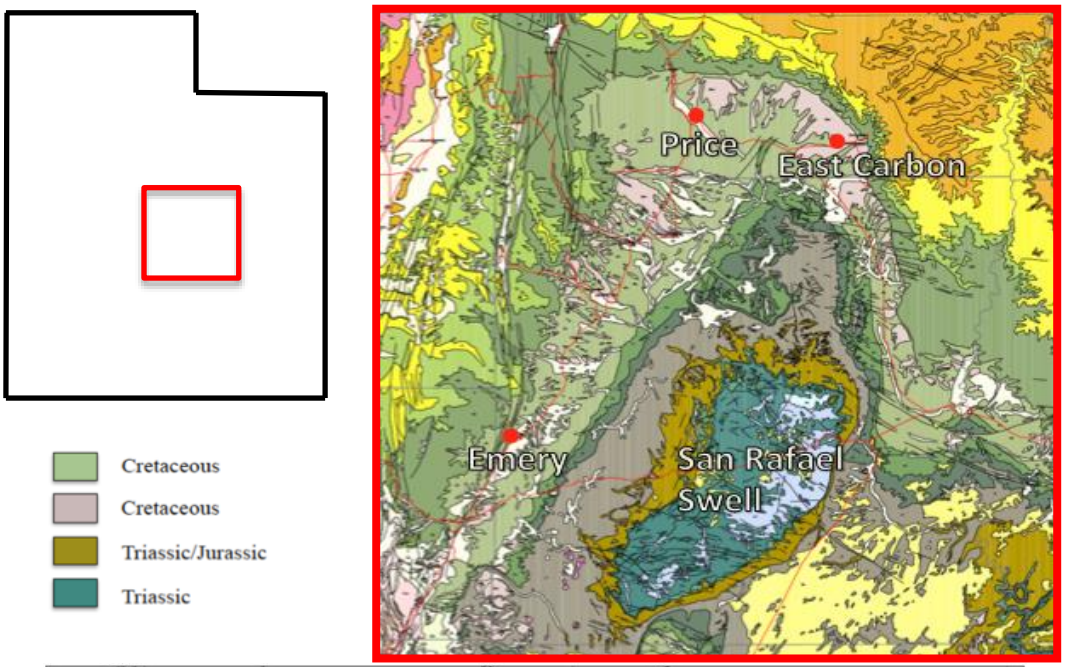

A

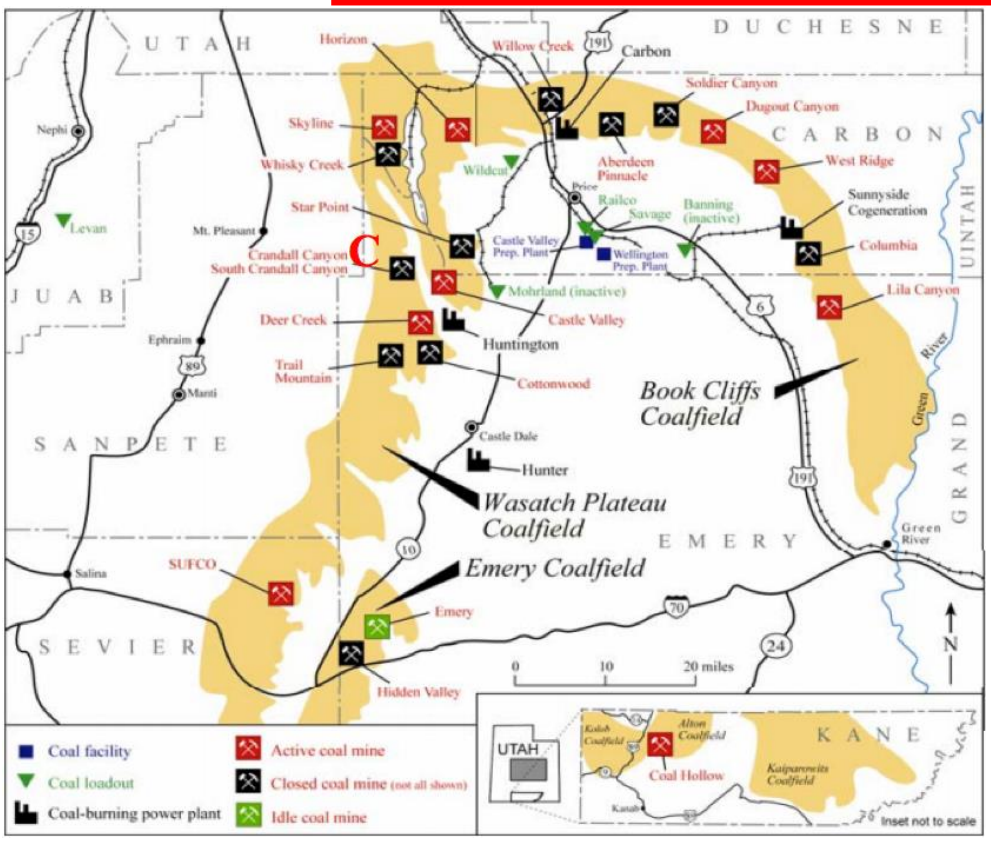

B

Figure 2: (A) Map of Utah, labeled with sample sites of Price, East Carbon, and Emery. The San Rafael Swell is labeled with I-70 bisecting it. Geological map from Utah Geological Society, http://geology.utah.gov/maps/geomap/statemap/index.htm). (B) Location of coal mines and associated industries in Utah. Samples for this study were collected from the Emery and Book Cliff Coalfields. Crandall Canyon Mine (marked with red "C") was closed in 2007 after a fatal mine roof collapse (MSHA, 2013). From Boden, et al., (2011).

four corners region (i.e. the boundary between Colorado, Utah, New Mexico, and Arizona), and covers about half of Utah (Davis and Bump, 2009). The units of relevance to this study include the Mancos Shale, the Ferron Sandstone and the younger Blackhawk Sandstone. The Ferron package contains sandstone, siltstone, 12 coal zones, and is exposed for ~56 km along the strike of the shallow-dipping western edge of the San Rafael Swell. To the north, the Ferron plunges below the Book Cliffs, and dips below the surface to the west (Stracher et al., 2005).

There are eight active coal mines in the study area, (nine in Utah) with four coal burning power plants. Utah produced 18.2 million tons of coal in 2011, valued at $660 million. However, only 17.0 million tons were distributed to market, with the rest stockpiled because of a decrease in demand caused by the recession (Boden et al., 2011). This high production highlights the amount of coal in the area, and thus the heightened susceptibility for coal fires, either through natural causes or human error in mining activity. Figure 2 also includes the location and status of the Utah coal mines, along with the associated facilities. It is also important to note the higher levels of mercury in the Emery coals, compared to the surrounding Wasatch Plateau and Book Cliffs coals (Fig. 3).

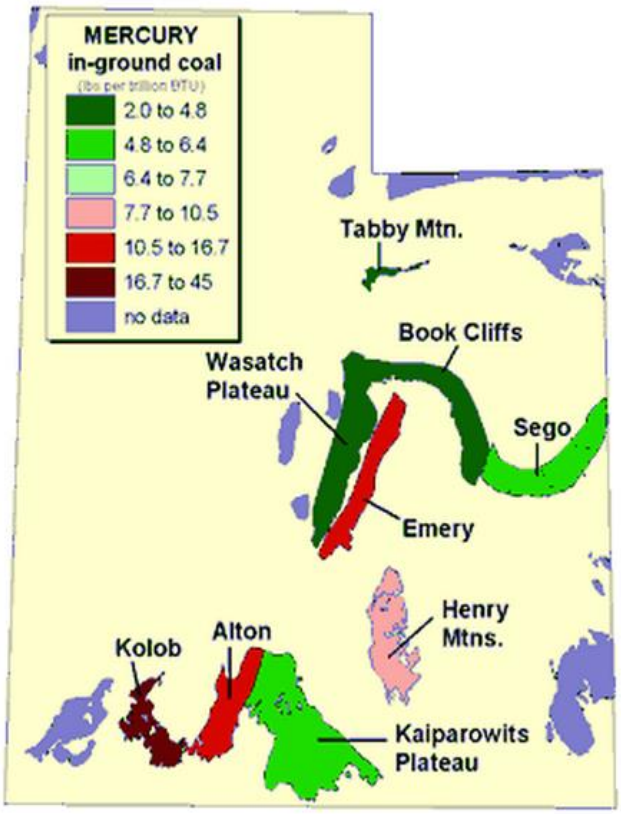

Figure 3: Mercury content of in-ground coal in Utah. Emery contains high mercury content, and thus perhaps has higher potential for leaching. Generally, the greater the sulfur content in the coal, the greater the mercury content in the coal, because pyrite is the main carrier of mercury (Yudovich and Ketris, 2005). From Quick (2005).

METHODS

Field and petrographic work was completed from the 9th–12th of July, 2013. Fifty-five samples were collected, including coal, unaltered sandstone, and paralava from the towns of East Carbon, Price, and Emery (Fig. 2). During field work, outcrops were examined and sampled in order to reflect the range of the clinker morphologies, colors, and textures. Samples depicting a rough stratigraphic column were collected at the Emery and Helper clinker outcrops to observe how distance above the burn zone varied. The samples are predominately fine-grained sandstone. Some of the paralava has brecciated pieces of altered slate or sandstone in it. Contacts were examined, along with possible chimneys above the coal seam that allow for the release of heat, pressure, and gas. The 20 m wide Helper roadcut showed intense pyrometamorphism and evidence of melted rock that was not seen as extensively elsewhere, and thus proposed to have experienced the highest grade of heat.

Thirteen thin sections were made for mineral identification and petrographic analysis. Billets were cut at Pomona College and sent to Spectrum Petrographics to be made into thin sections. Thin sections were examined at Pomona College using a Leica Model DME Petrographic Microscope. Thin section photomicrographs were taken using a Leica ICC50HD microscope in conjunction with LeicaAquire software.

Scanning electron microscope (SEM) analysis was used to examine minerals and mineral intergrowths at high magnification to determine elemental distribution within individual grains, mineral assemblages, and crystal formation history. Samples were carbon coated and examined using Pomona College's Hitachi SU-70 SEM. SEM measurements were taken at 15–20 kV of accelerating voltage, 33–40 mA, with working distances of 10-–13 mm. In addition, elemental composition data was gathered using energy dispersive spectroscopy (EDS).

X-ray diffraction (XRD) was used to identify minerals in original and metamorphosed samples. XRD measurements were taken at 10–65º, 60 minute counting time, on 40 kV and mA current of 44, on Bragg Brentano configuration. X-ray fluorescence (XRF) analysis identified major and minor elements. XRF bead preparation and analytical conditions follow those reported by Johnson et al. (1999; Lackey et al., 2012). Beads were analyzed on Pomona College's PANalytical Axios XRF.

RESULTS

Field Relations

The East Carbon, UT study area contains three main sites: 1) Sunnyside, 2) Horse Canyon, and 3) Soldier Creek mine. The Sunnyside field area (39º33'35.568"N, 110º22'20.238"W) is ~5 km NE along Hwy 123 to the northeast of the town of East Carbon. The coal seam that would have directly pyrometamorphosed this deposit is not visible, but may be underground. In this area, as well as other field locations to the south and west, the Blackhawk sandstone dips away from the center of the San Rafael Swell (Fig. 2). Coal seams are visible across the valley in this area, and other unreachable clinker locations about 60 m up are also visible in the prominent cliff exposures. Figure 4 is a view of clinker deposits within the cliffs, and shows burned and original sandstones. The burning of coal decreased the volume, thus causing some collapse of the outcrop, however the thick sequence of sandstones appears relatively intact. This lack of collapse may be a consequence of the coal seam being relatively thin, or the mechanical strength of the formation above that prevented the sequence from causing widespread collapse. The overall stratigraphy of this area is intact, with Mesa Verde sandstone visible. Though the steep nature of the cliffs makes potential sites difficult to sample, there is an accessible sandstone clinker deposit across Hwy 123 and the cliffs of Figure 4, with samples taken from different areas in the burned stratigraphy (Fig. 5). The outcrop showed variable color and allowed for sampling relatively close to the bottom of the Blackhawk formation, in an area close to a presumed coal seam. The exposed outcrop area is ~6 m high and 12 m wide. The samples from this area are altered sandstones, ranging in color from dark grey, to red, to yellowish. Samples 13UT-5 through -10 were collected in situ vertically up the outcrop (Fig. 6), with 13UT-5 being closest to the assumed underground coal seam. 13UT-12 is a yellow loose medium grained sandstone sample found below the sample column. The samples range from grey medium-grained siltstone (13UT-5, -8), red medium-grained siltstone (13UT-7, -10), to a pink, subrounded fine-grained sandstone (13UT-9).

Horse Canyon is located south of East Carbon and off of U.S. 124 (39º27'39.668"N, 110º21'12.966"W). There are a series of abandoned buildings in this area. Horse Canyon shows a similar style to Sunnyside of steep cliffs. There was accessible clinker deposit up on a hill that was not covered by vegetation (Fig. 7). This exposed burn area is ~12 m high and ~40 m across. There is no visible coal seam for source of burn. Again, there are areas of altered and unaltered sandstone visible across the road on cliff faces (Fig. 8).

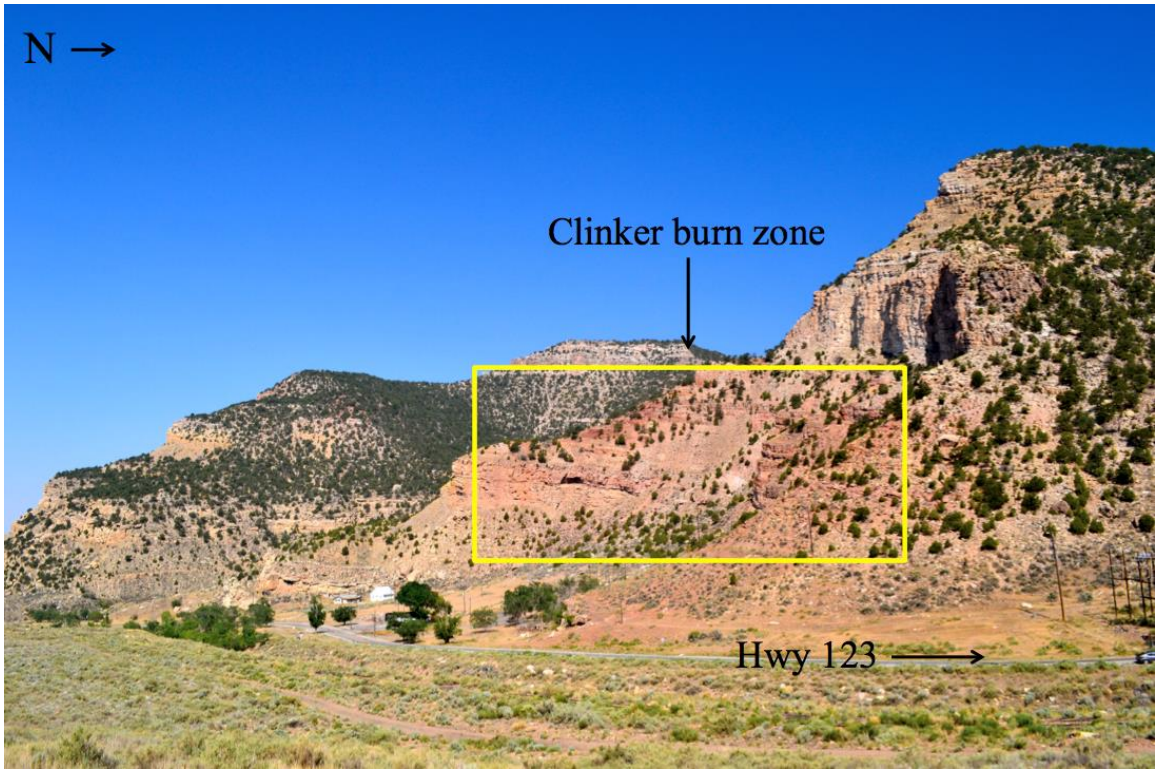

Figure 4: View from East Carbon outcrop in Figure 5. Typical red clinker, which decreases upwards in color intensity. However, no visible coal seams are present. Note house for scale.

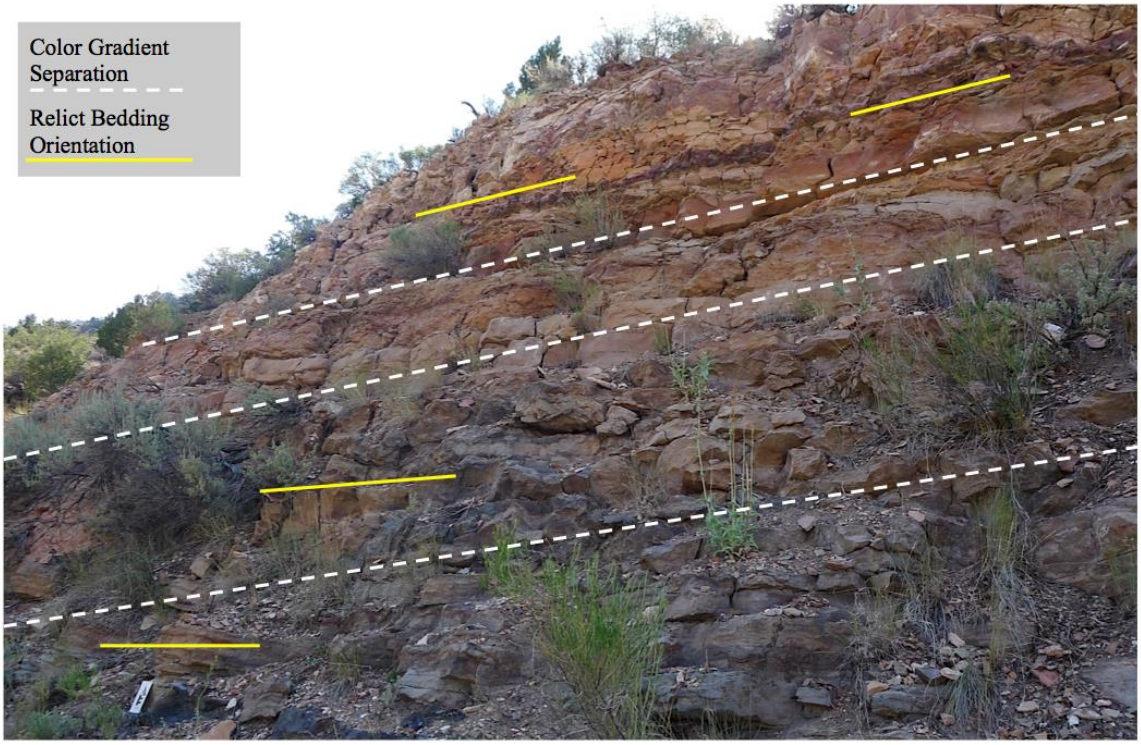

Figure 5: Annotated outcrop from East Carbon showing variation in color, possibly due to differences in heat. Relict bedding is notated by yellow lines.

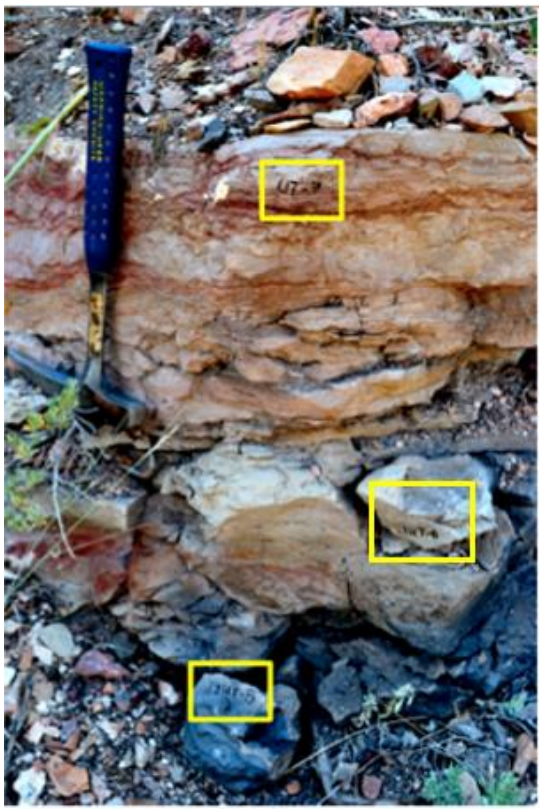

Figure 6: East Carbon samples 13UT-5 through -7 collected in situ. Hammer for scale (20 cm).

Figure 7: Horse Canyon sample 13UT-15 collected in situ. Sledge hammer for scale (25 cm).

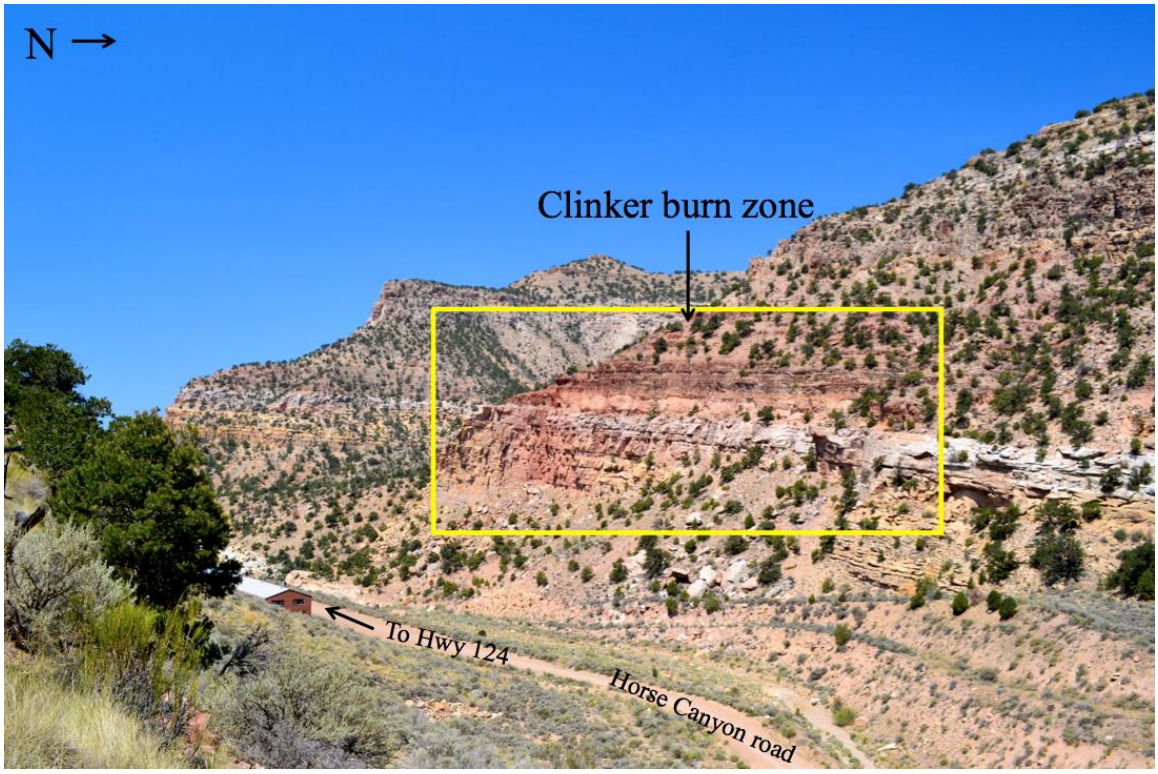

Figure 8: View across Horse Canyon Road from outcrop in Figure 7. Clinker deposit with characteristic red coloring, but no visible coal seam.

The third outcrop in the East Carbon area is the defunct coal mine Soldier Canyon Mine (39º42'01.563"N, 110º36'40.425W). This burn area is ~8 m high and ~35 m wide. There are three condemned mine shafts visible, with the burned sandstone sample (13UT-16) collected near mine shaft 1 (Fig. 9)

The Helper field area is located on Hwy 191, past an active coal power plant. The clinker roadcut is ~18 m tall and ~50 m wide, with varying shades of yellows, reds, whites, black, greys, blue-greens, and greens (Fig. 10). Some of the yellow colored samples has preserved bedding present. Vesicular paralava is present in black and green shades. Some samples have large vesicles, up to 3 cm. There are four possible natural chimneys in this outcrop, as annotated in Figure 10. These chimneys have cool air coming out of them, possibly indicating a connection to a mine shaft or evacuated space underground. The chimneys appear filled with brecciated rocks and melt, and may be collapsed into themselves. Some of the green paralava is smooth, with no vesicles flow and drip structures. Figure 11 shows the diverse paralava appearance, including samples with brecciated burned sandstone contained within them. Samples were taken from the chimney areas, in addition to a series of altered sandstone samples (UT13-17- through -20) taken from a variety

Figure 9: Defunct Soldier Canyon Coal Mine. Red clinker visible above entrances to mine shafts. Sample 13UT-16 collected by Mine Shaft 1.

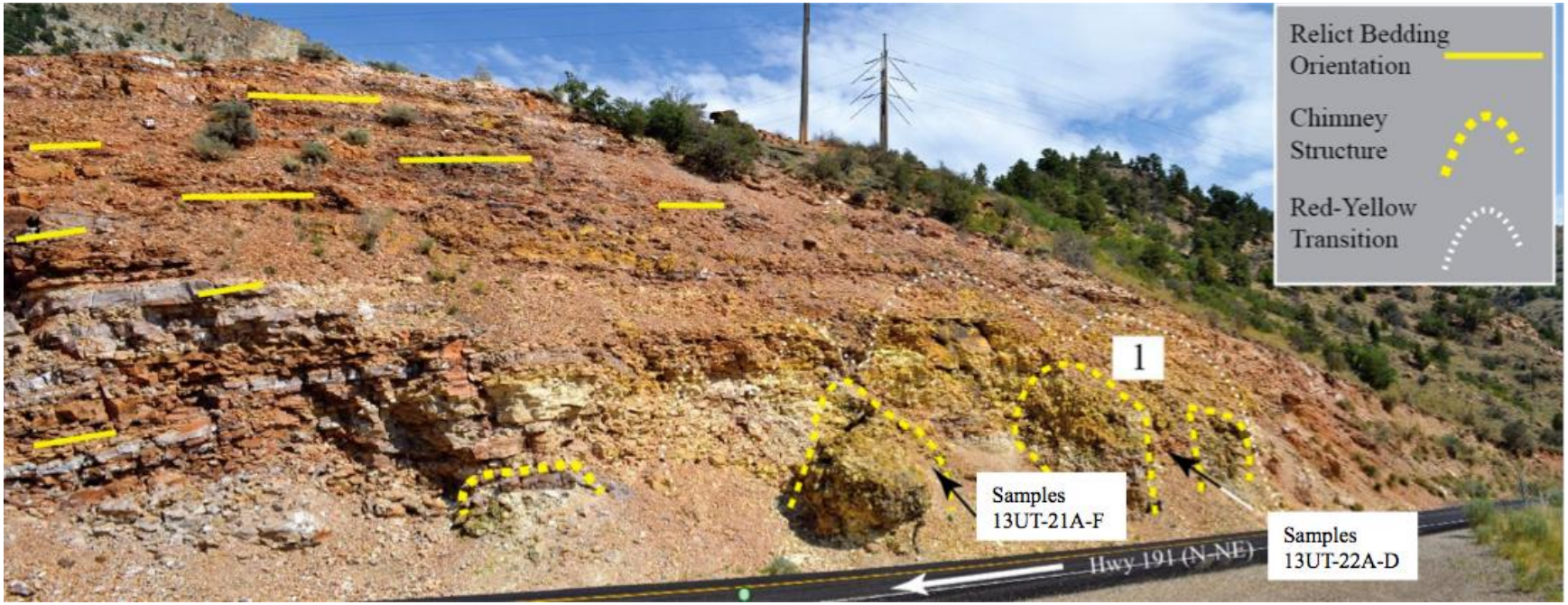

Figure 10: Annotated outcrop near Helper. Outcrop is ~18 m high. There are four visible chimney structures, indicated by a dashed yellow line. Solid yellow lines indicate relict bedding orientation, and the dotted white line shows color transition of outcrop between red and yellow. Paralava samples 13UT-21A–F and 12UT-22A–D were collected from two different chimney structures. The chimney marked with a "1" designates where the pictures in Figure 11 were taken.

Figure 11: Sample of paralava textures from Helper roadcut. (A) depicts a green, vesicle-rich melt; (B) shows a contact between the orange baked sandstone and the melt below; (C) is a possible chimney vent (seen in the shadows) and conceivably had the highest temperatures for this unit; (D) depicts brecciated, baked sandstone within the paralava. Lens cap is 4.0 cm for scale.

of colors in a vertical column of the outcrop (Fig. 12). Sample 13UT-17 is a medium-grained yellow sandstone, as is 13UT-18A, but has layers of yellow and white material. 13UT-19 is a creamy-white, coarse-grained siltstone. 13UT-20 appears to have a small amount of black colored vesiculated melt attached to the red, coarse-grained siltstone. 13UT-23B and -23C are grey, medium-grained sandstones found near the same area as samples 13UT-17 through -20. The paralava and melt samples are glassy to crystalline rock, and are dominated by new crystals. Some of these paralava samples are vesiculated, with size of vesicles ranging from 1-5 mm.

The field site is located south of the town of Emery (38º49'32.768"N, 111º12'19.245"W). This area has laterally extensive and thick (up to 220 m) deposits of Mancos shale underlain by the Ferron sandstone (Fig. 13A). This field area is in the lower Mancos shale, deposited by the Cretaceous Western Interior Seaway. There is a visible change from original to metamorphosed sandstones. The samples were not collected in situ, as the burned area is too high and inaccessible. Loose samples were collected from talus at the base of the cliffs. Mostly red boulders have fallen, however Figure 13B illustrates the variety of color in the detritus. Sample 13UT-24A is a red, medium-grained sandstone.

Other samples were collected south of Emery out on a plateau (38º52'07.572"N, 111º13'47.391"W). Most of the visible sandstones in this area are red, though there is still some variation in color. Following Coal Seam Road, there are visible coal seams, ranging from 1-5 m thick, and overlain with sandstone. There is also a grey fine-grained siltstone that has been baked. Across the canyon from Coal Seam Road, there are three visible coal seams (Fig. 14) that become thinner up section. Samples of altered and unaltered sandstones were collected on plateau. Sample 13UT-28A has distinct color differentiation, with layers (2 mm–15 mm thickness) of alternating white and brick red. Samples 13UT-25 through -30B were collected on top of the plateau. Sample 13UT-27 is a creamy colored, fine-grained sandstone. Unaltered, medium-grained sandstone samples include 13UT-29 and -30B. 13UT-30A is a red, baked, medium-grained sandstone with visible layering of color differentiation.

Whole Rock Geochemistry

XRF analysis for samples from Sunnyside (Samples 13UT-5 through -12 in Table 1) reveal low concentrations of alkalis, with only 0.03 wt.% Na_2O recorded for sample 13UT-9, a reddish colored baked sandstone. The highest concentration for CaO 6.83 wt.% for sample 13UT-9, a grey sandstone. Sample 13UT-10, a bright red sandstone, has the highest concentration of Fe_2O_3, at 19.19 wt. % (Fig. 15A). Throughout the sample column, Al_2O_3 decreases higher above the inferred coal seam, until 13UT-10 when concentrations spike (Fig. 15B). Sample 13UT-15 was collected in

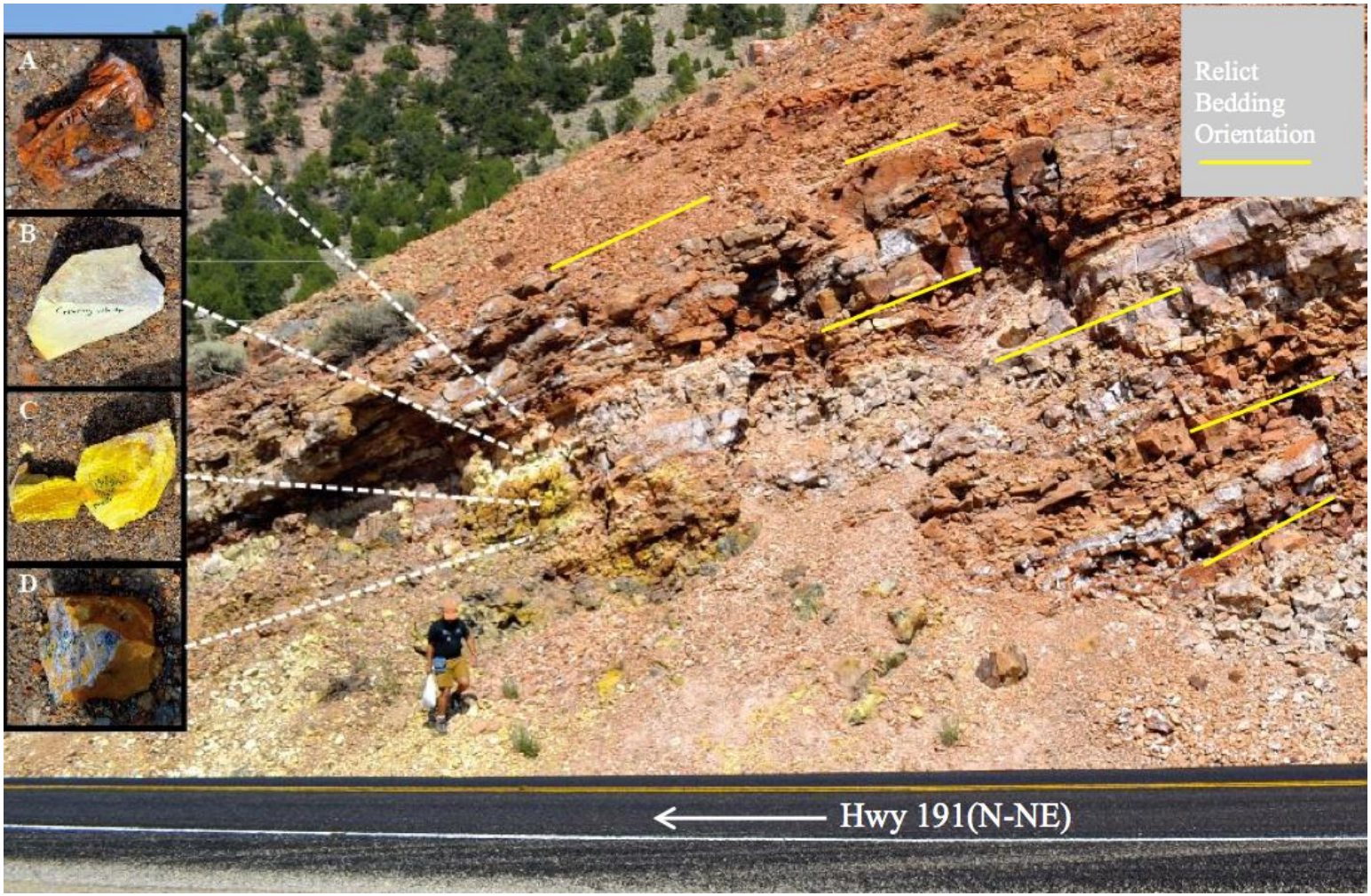

Figure 12: Continuation of Helper outcrop, moving further north. Samples 13UT-17–20 were collected in a vertical transect noted on figure: (A) 13UT-20; (B) 13UT-19; (C) 13UT-18; (D) 13UT-17. Solid yellow lines indicate relict bedding orientation. Note the bedding here is sloping steeper than in Figure 11.

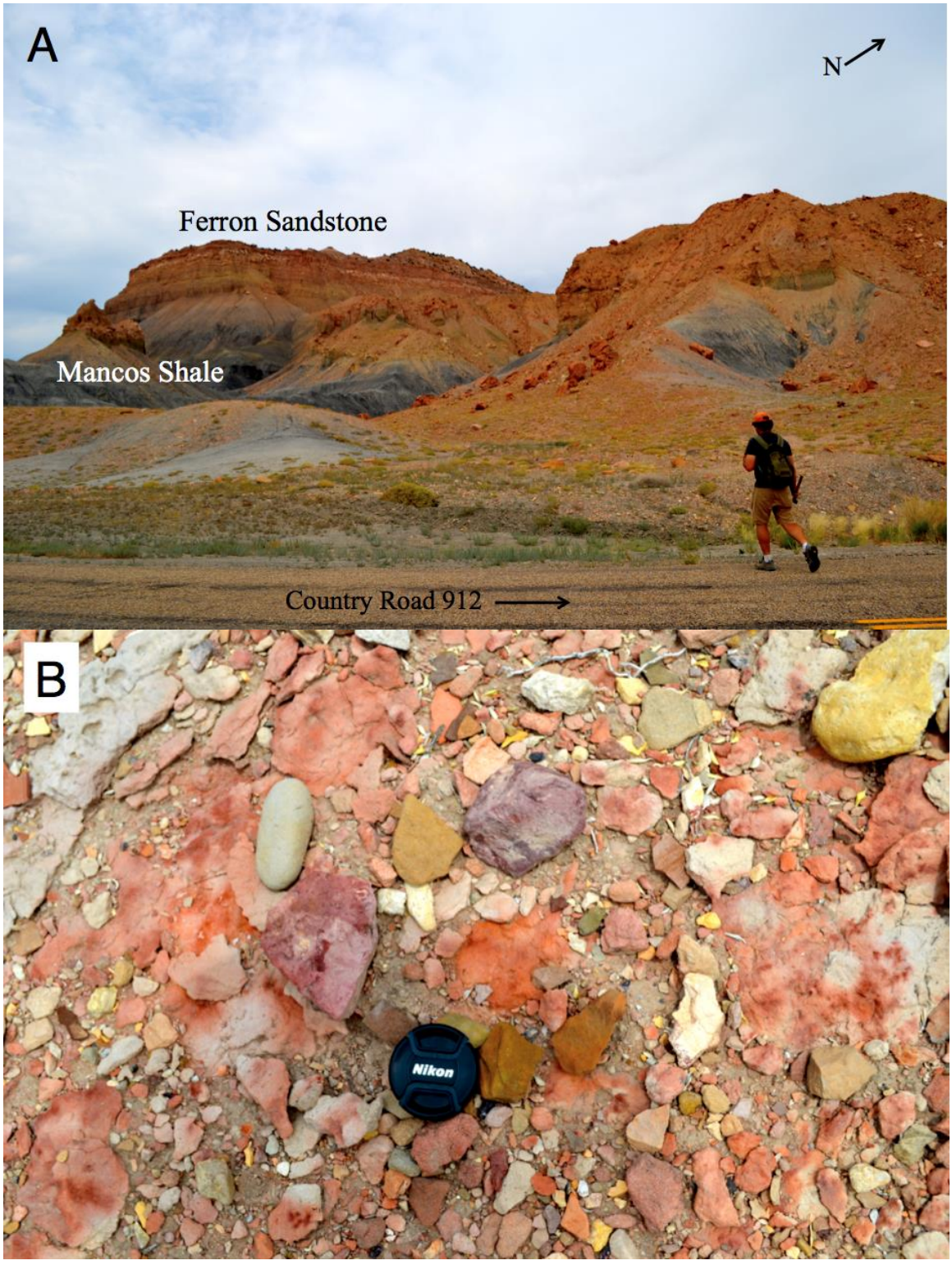

Figure 13: (A) Field photo from Emery showing the burned Ferron sandstone clinker acting as a weathering-resistant cap rock overlying the Mancos Shale. (B) Detrital material from Ferron sandstone. Lens cap for scale, 4.0 cm.

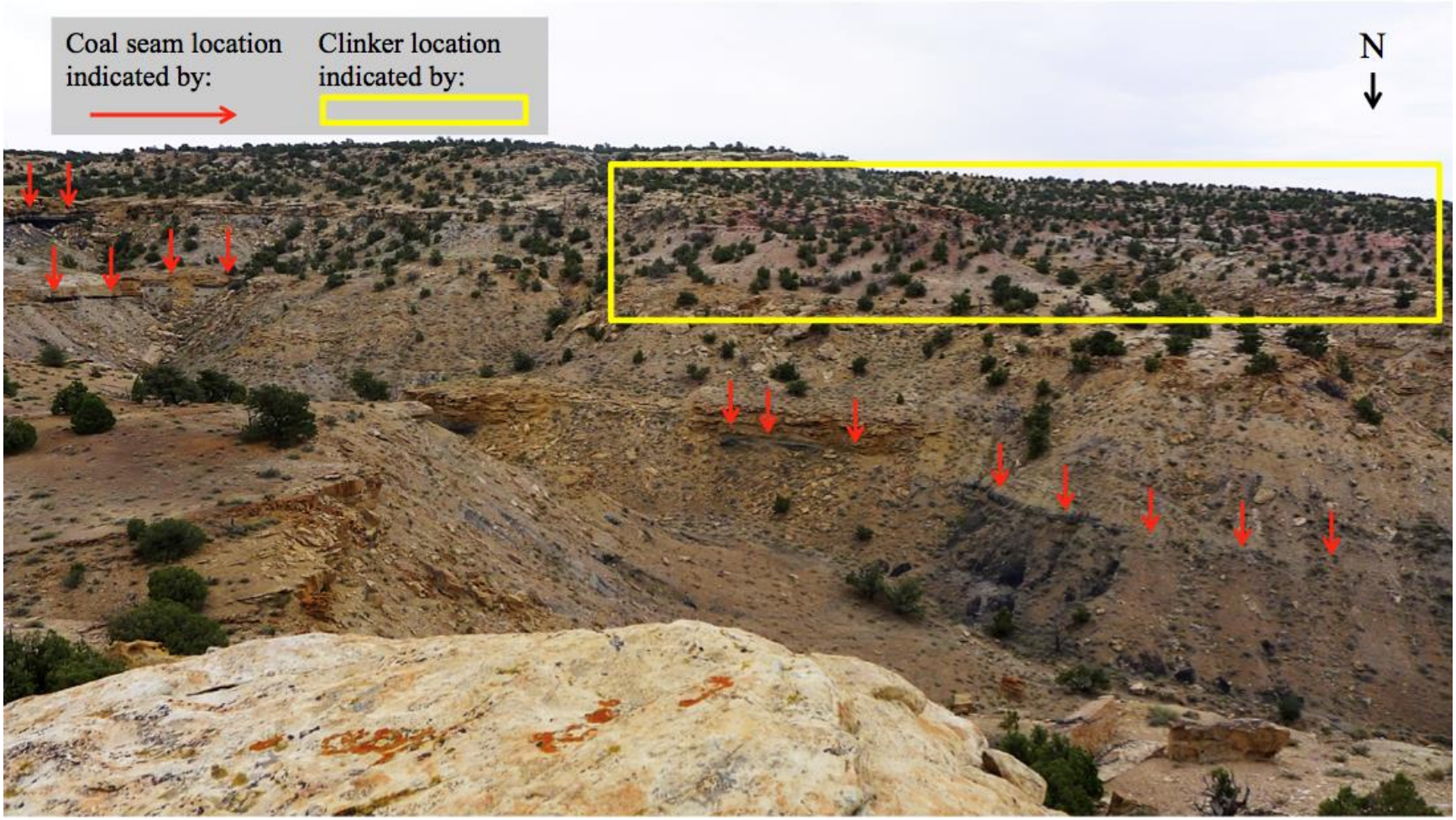

Figure 14: Coal seams visible on Emery plateau, indicated by red arrows pointing to the seams. Red clinker is highlighted by a yellow box. The sequence of coal seams overlain by sandstone signifies a shift from a swamp to a sandy environment, and thus shallower seas.

TABLE 1: XRF DATA FOR EAST CARBON, UT

SAMPLE	SiO_2	TiO_2	Al_2O_3	Fe_2O_3	MgO	MnO	CaO	K_2O	Na_2O	P_2O_5	Zr	Cu
13UT-5	74.13	0.61	11.51	1.32	0.84	0.01	1.20	2.20	0.11	0.32	295.40	15.30
13UT-6	72.13	0.64	12.79	0.87	0.72	0.00	0.45	2.20	0.09	0.11	283.30	17.30
13UT-7	79.68	0.55	9.14	1.11	0.65	0.02	0.94	1.87	0.05	0.22	402.80	5.80
13UT-8	81.34	0.33	4.97	1.03	0.63	0.02	1.72	0.99	0.11	0.20	330.30	2.90
13UT-9	76.24	0.16	2.60	1.05	0.78	0.03	6.83	0.60	0.03	0.12	194.90	bdl
13UT-10	58.69	0.48	8.61	19.19	1.57	0.38	1.43	1.47	0.02	0.30	230.50	14.50
13UT-12	79.19	0.49	7.85	0.98	0.60	0.02	1.00	1.63	0.05	0.20	421.00	4.30
13UT-15	68.26	0.10	1.15	1.34	1.72	0.05	11.40	0.30	0.00	0.09	191.40	bdl
13UT-16	38.12	0.03	0.41	1.87	7.91	0.03	21.31	0.13	0.00	0.04	39.40	bdl

All oxides in weight percent; All other elements in parts per million (ppm). Below detection limit abbreviated to “bdl”.

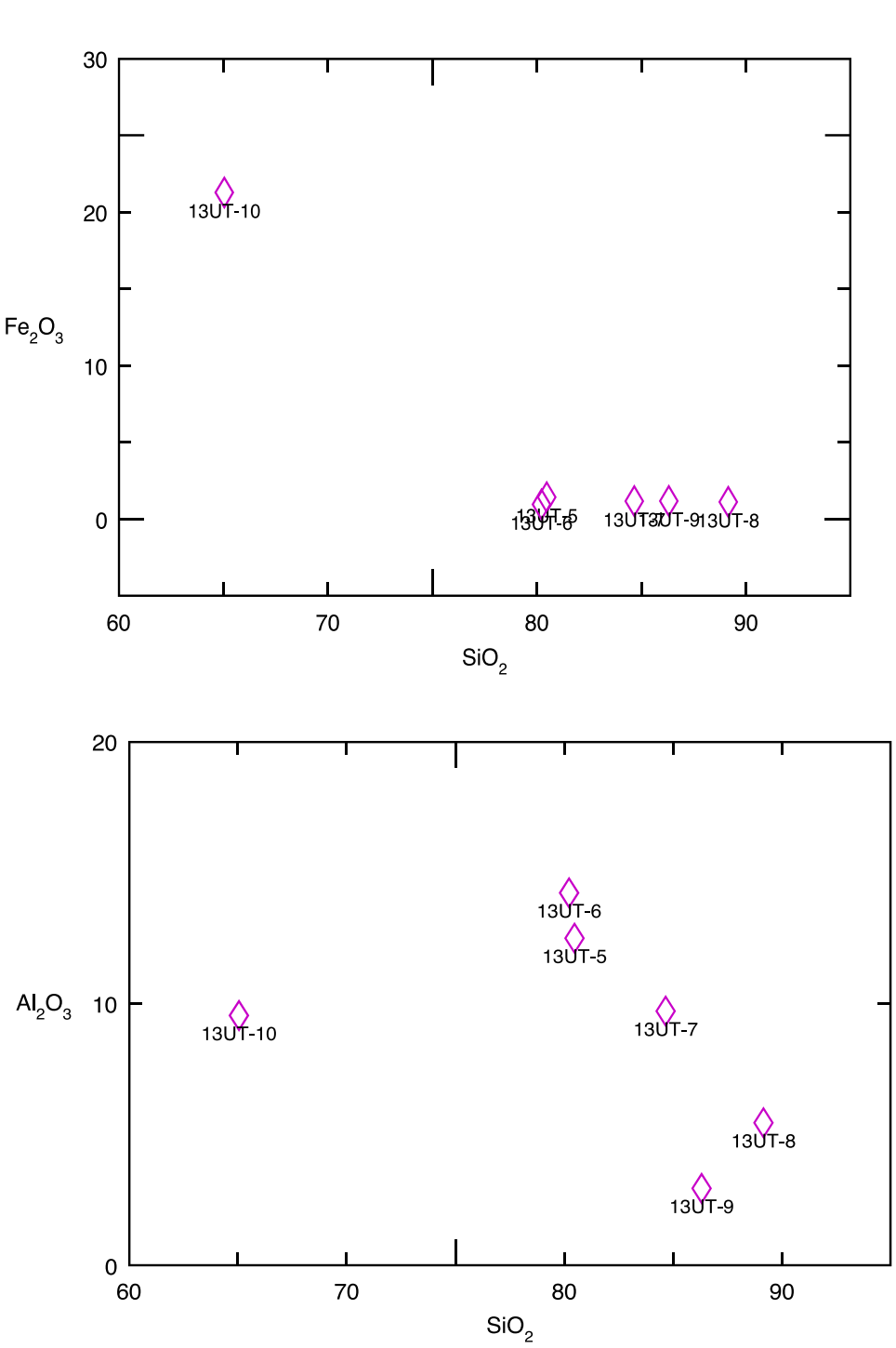

Figure 15: (A) Plot of Fe_2O_3 vs SiO_2. Sample 13UT-10 has anomalously high iron content compared to rest of samples from transect. (B) Plot of Al_2O_3 vs SiO_2. Not very much variation in Al, but highlights depletion of SiO_2 for 13UT-10.

Horse Canyon, and its XRF analysis is also found in Table 1. This sample contains even lower alkali content than the previous sample area. XRF analysis for sample 13UT-16 from Soldier Canyon Mine reveals the lowest SiO_2, Al_2O_3, and Zr content within the East Carbon suite of samples, but the highest CaO concentration.

Table 2 contains representation of elemental concentrations for Helper. The XRF analysis for the vertical sampling of the sandstones at Helper shows 13UT-20 being the most anomalous. A section of the sample appears to be a black, vesicular melt, and a piece of this melt (13UT-20V) was analyzed in addition Figure 16A depicts CaO concentrations, with 13UT-20 being much lower. Figure 16B is a graph of Al_2O_3 concentration vs. SiO_2, again showing 13UT-20 being off trend. However, the other three samples show a liner trend of decreasing SiO as Al_2O_3 increases moving up the outcrop. All of the Helper samples were plotted together to look for geochemical connections between paralava and clinker. Figure 17B depicts SiO_2 vs. MgO and shows enrichment of MgO as SiO_2 depletes, despite the clinker (filled red circle) following similar trends to green melts (open red circle). Sample 13UT-21F has the lowest CaO, MgO, and Al_2O_3 concentrations, but the highest SiO_2. Figure 17A again shows depletion of SiO_2, but enrichment of CaO trend. For Fe_2O_3 (Fig. 17C), there is a less defined trend, and no correlation between clinker and melt. XRF analysis for Emery samples 13UT-24A and -24C show few trends in concentrations of major elements and traces (Table 3). 13UT-24C has the lowest SiO_2 content and highest Al_2O_3 and TiO_2 for any Emery sample. Samples 13UT-27 to -30B show similar values for SiO_2. However, 13UT-25 contains the lowest SiO_2 concentration for any Emery sample, and the highest MgO concentration. Complete XRF data for all samples can be found in Appendix A.

Mineralogy, Microtextures, and Phase Relations

XRD analysis of the Sunnyside samples showed similar results, with abundant quartz. As shown in Figure 18A–D, samples 13UT-5 through -8 depict typical quartz spectra. However, sample 13UT-9 shows calcite as well as quartz (Fig. 18E), and 13UT-10 depicts hematite in addition to quartz (Fig. 18F). These minerals reflect the relatively high values of CaO and Fe_2O_3 for these two samples. The XRD spectrum for 13UT-15 from Horse Canyon (Fig. 19A) show quartz, dolomite ($CaMg(CO_3)_2$), and calcite ($CaCO_3$), which would explain the elevated CaO concentrations. The XRD spectra for Soldier Canyon Mine indicates the same minerals as 13UT-15 (Fig. 19B). XRD analysis of the paralavas at Helper show distinct spectra from the quartz dominated sandstones (Fig. 20). However, because of the high glass content, these spectra have higher background noise than other samples. These sandstones contain diopsidic pyroxene, giving the samples their distinct green color.

TABLE 2: XRF DATA FOR HELPER, UT

SAMPLE	SiO_2	TiO_2	Al_2O_3	Fe_2O_3	MgO	MnO	CaO	K_2O	Na_2O	P_2O_5	Zr	Cu
13UT-17	56.04	0.11	1.94	3.42	8.38	0.07	19.72	0.59	0.00	0.10	127.30	10.30
13UT-18A	41.71	0.15	2.69	2.93	6.82	0.06	16.35	0.71	0.00	0.10	114.20	bdl
13UT-19	51.04	0.46	8.86	1.80	6.26	0.06	19.16	2.00	0.06	0.24	176.50	21.60
13UT-20	66.89	0.78	18.56	2.16	1.56	0.00	1.46	3.20	0.11	0.39	174.10	39.90
13UT-20V	64.94	0.69	15.50	1.51	1.87	0.01	4.26	3.09	0.12	0.35	147.30	22.80
13-UT-21A	60.53	0.60	11.55	2.98	4.35	0.08	13.65	2.32	0.12	0.33	220.30	48.30
13UT-21A.2	60.32	0.59	11.44	2.96	4.03	0.07	12.70	2.33	0.06	0.32	221.90	19.10
13-UT-21B	51.85	0.48	8.74	4.14	7.59	0.09	21.87	1.82	0.07	0.27	195.70	13.40
13-UT-21C	60.25	0.59	11.20	3.55	4.35	0.08	13.85	2.22	0.08	0.32	223.30	27.00
13-UT-21E	59.71	0.58	11.47	2.50	4.44	0.06	13.44	2.58	0.13	0.29	183.20	16.20
13UT-21F	82.61	0.44	6.86	0.35	0.39	0.00	0.01	0.88	0.03	0.02	283.90	bdl
13-UT-21G	47.60	0.44	8.65	2.81	8.82	0.09	25.98	1.87	0.05	0.25	154.00	16.20
13-UT-21I	59.68	0.59	11.52	3.17	4.24	0.08	13.34	2.26	0.12	0.32	217.10	32.10
13-UT-22B	56.75	0.48	8.84	2.22	7.21	0.06	18.67	1.90	0.05	0.25	216.50	23.70
13-UT-22D	50.34	0.43	8.28	2.07	9.54	0.06	25.04	1.62	0.06	0.23	198.90	12.90
13-UT-22E	56.70	0.47	8.57	2.12	7.72	0.06	19.53	1.82	0.04	0.25	220.30	22.20
13UT-23B	74.59	0.07	1.62	2.25	1.32	0.07	7.62	0.28	0.02	0.19	66.20	bdl
13UT-23C	71.34	0.06	1.51	2.30	1.61	0.08	8.28	0.34	0.06	0.19	60.60	bdl

All oxides in weight percent; All other elements in parts per million (ppm). Blow detection limit abbreviated to “bdl”.

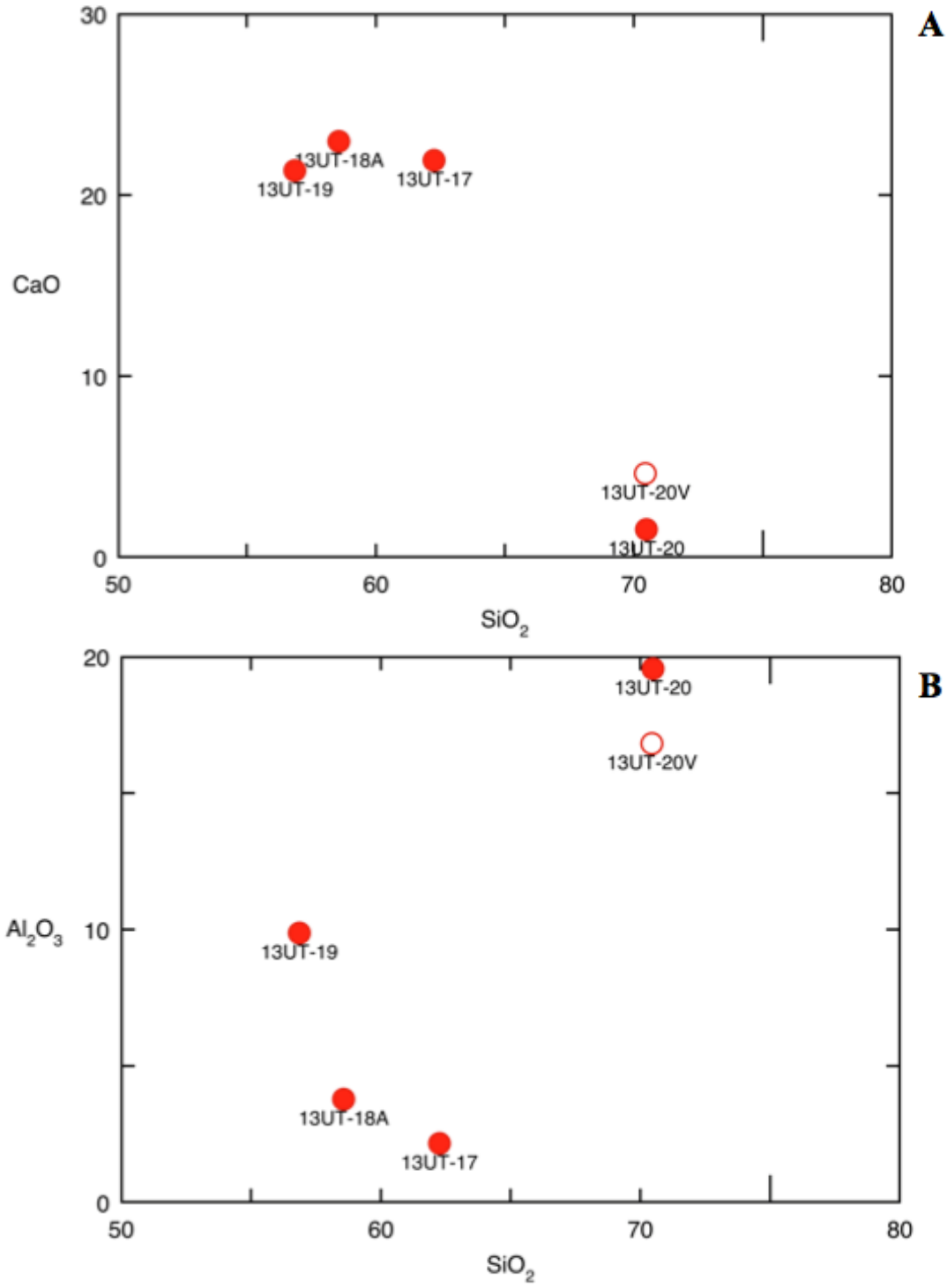

Figure 16: (A) Plot of clinker samples from transect. 13UT-20V is a melt sample from 13UT-20, which is depleted in CaO compared to the other samples. (B) Plot of Al_2O_3 showing enrichment in Al for 13UT-20.

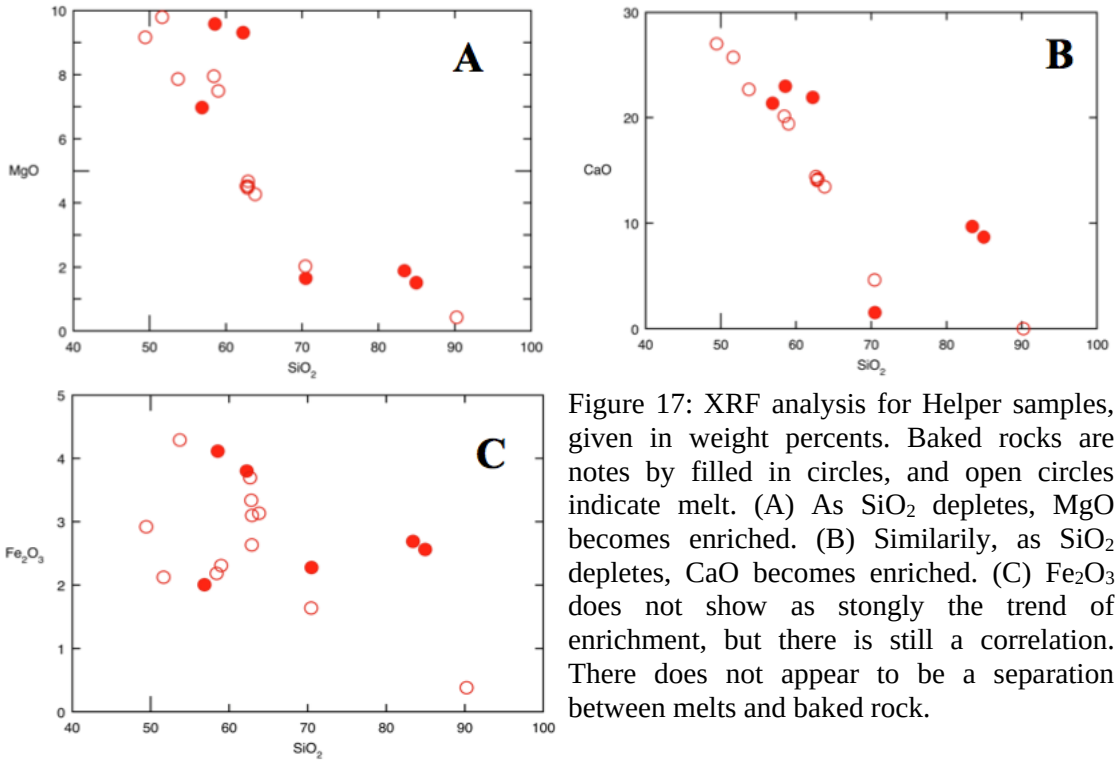

Figure 17: XRF analysis for Helper samples, given in weight percents. Baked rocks are notes by filled in circles, and open circles indicate melt. (A) As SiO_2 depletes, MgO becomes enriched. (B) Similarily, as SiO_2 depletes, CaO becomes enriched. (C) Fe_2O_3 does not show as stongly the trend of enrichment, but there is still a correlation. There does not appear to be a separation between melts and baked rock.

TABLE 3: XRF DATA FOR EMERY, UT

SAMPLE	SiO_2	TiO_2	Al_2O_3	Fe_2O_3	MgO	MnO	CaO	K_2O	Na_2O	P_2O_5	Zr	Cu
13UT-1	83.68	0.27	5.56	2.48	0.05	0.00	0.21	1.47	0.54	0.06	315.70	bdl
13UT-4	82.51	0.09	5.44	2.28	0.04	0.00	0.60	1.10	0.52	0.05	63.70	12.50
13UT-24A	80.57	0.26	4.96	1.69	1.15	0.02	1.81	1.24	0.46	0.08	350.60	bdl
13UT-24C	58.94	0.99	23.86	5.64	1.01	0.06	1.37	0.82	0.14	0.04	190.10	30.20
13UT-25	47.57	0.50	9.65	6.70	7.68	0.14	19.55	2.37	0.08	0.27	161.10	16.00
13UT-27	71.12	0.21	7.66	10.21	0.10	0.00	0.19	2.06	0.60	0.13	119.20	bdl
13UT-28A	82.97	0.16	6.76	1.00	0.06	0.00	0.07	2.27	0.60	0.03	206.40	bdl
13UT-28B	81.13	0.39	5.65	2.93	0.27	0.06	0.19	0.94	0.03	0.09	430.50	13.00
13UT-28C	82.16	0.22	7.01	1.02	0.16	0.04	0.39	1.76	0.59	0.05	218.70	8.30
13UT-28E	86.15	0.21	4.32	0.22	0.08	0.00	0.38	1.08	0.32	0.02	324.60	bdl
13UT-29	85.91	0.23	4.00	0.89	0.28	0.00	0.49	1.17	0.45	0.02	212.60	bdl
13UT-30A	79.91	0.18	6.74	0.81	0.92	0.01	0.49	1.09	0.72	0.04	82.70	bdl
13UT-30B	80.68	0.14	3.55	1.40	0.96	0.01	2.73	0.44	0.17	0.04	110.10	1.30

All oxides in weight percent; All other elements in parts per million (ppm). Blow detection limit abbreviated “bdl”.

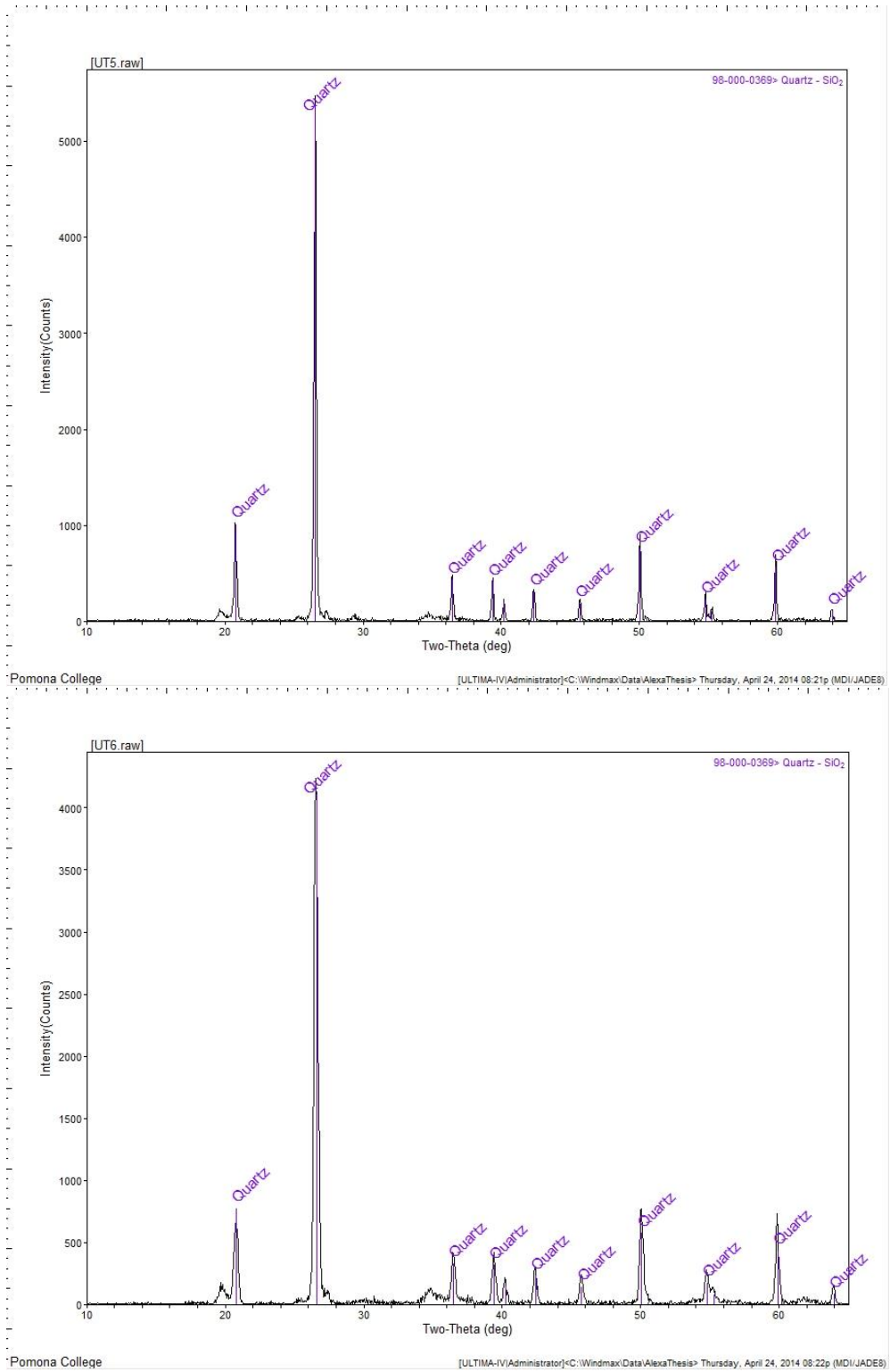

Figure 18: XRD spectra of samples from East Carbon, all depicting typical quartz peaks. (A) Sample 13UT-5; (B) Sample 13UT-6.

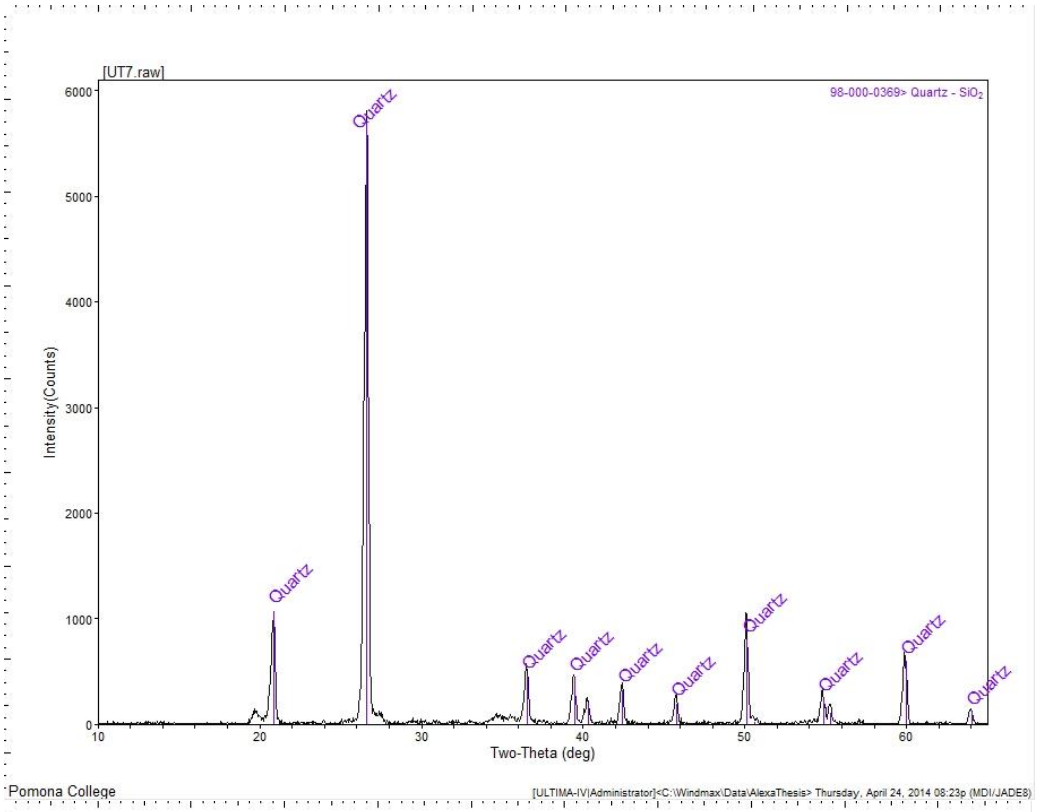

C

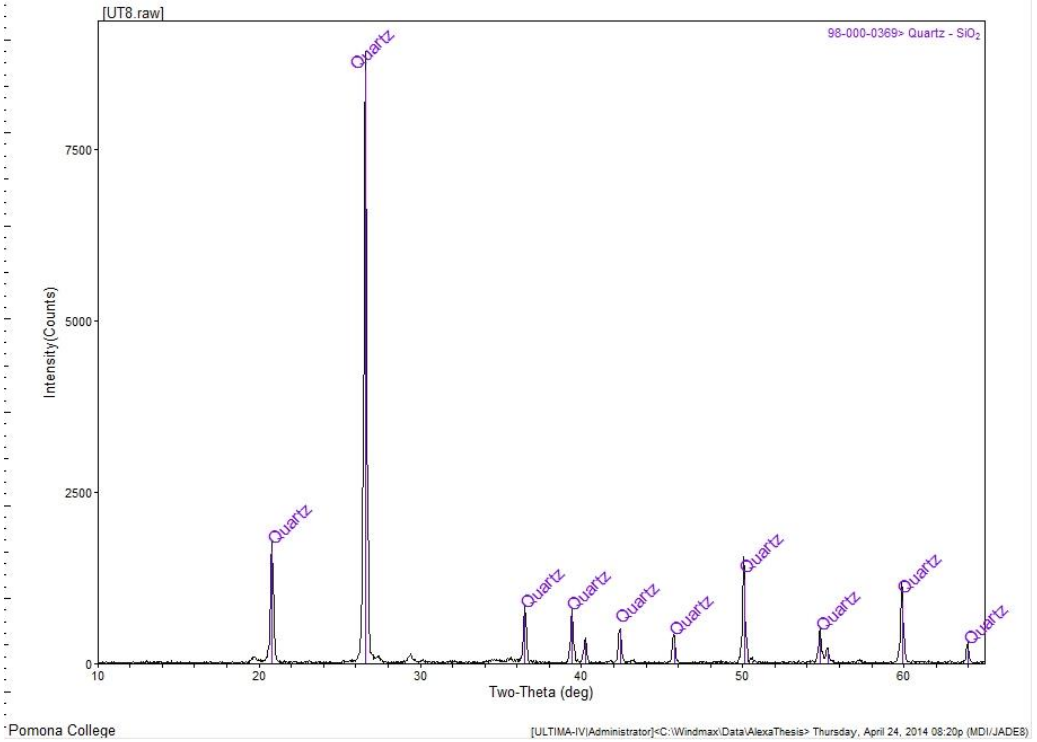

D

Figure 18 (Continued): Quartz dominated XRD spectra from East Carbon. (C) Sample 13UT-7; (D) Sample 13UT-8.

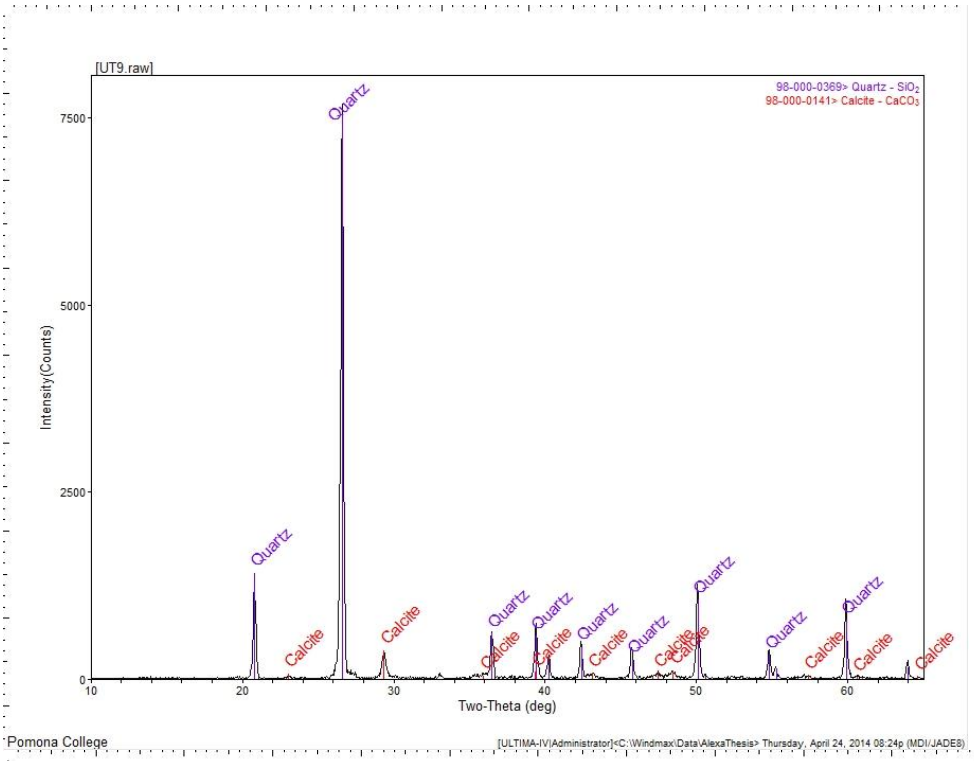

E

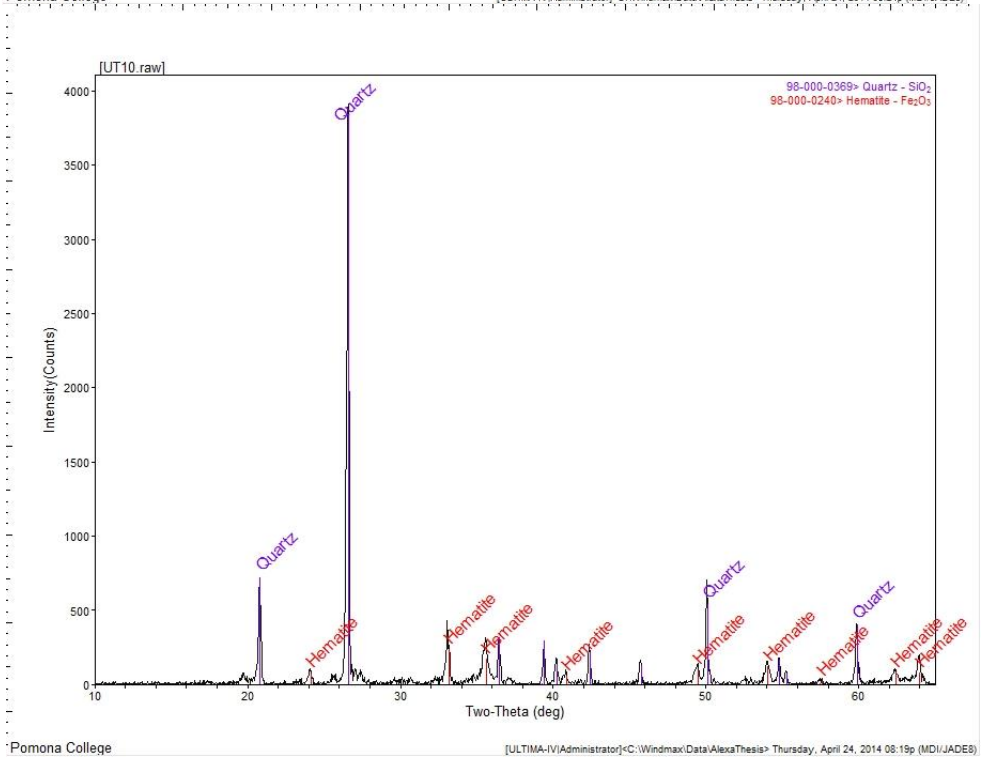

F

Figure 18 (Continued): Quartz dominated XRD spectra from East Carbon. (E) Sample 13UT-9 with calcite in addition to quartz; (F) Sample 13UT-10 also contains hematite.

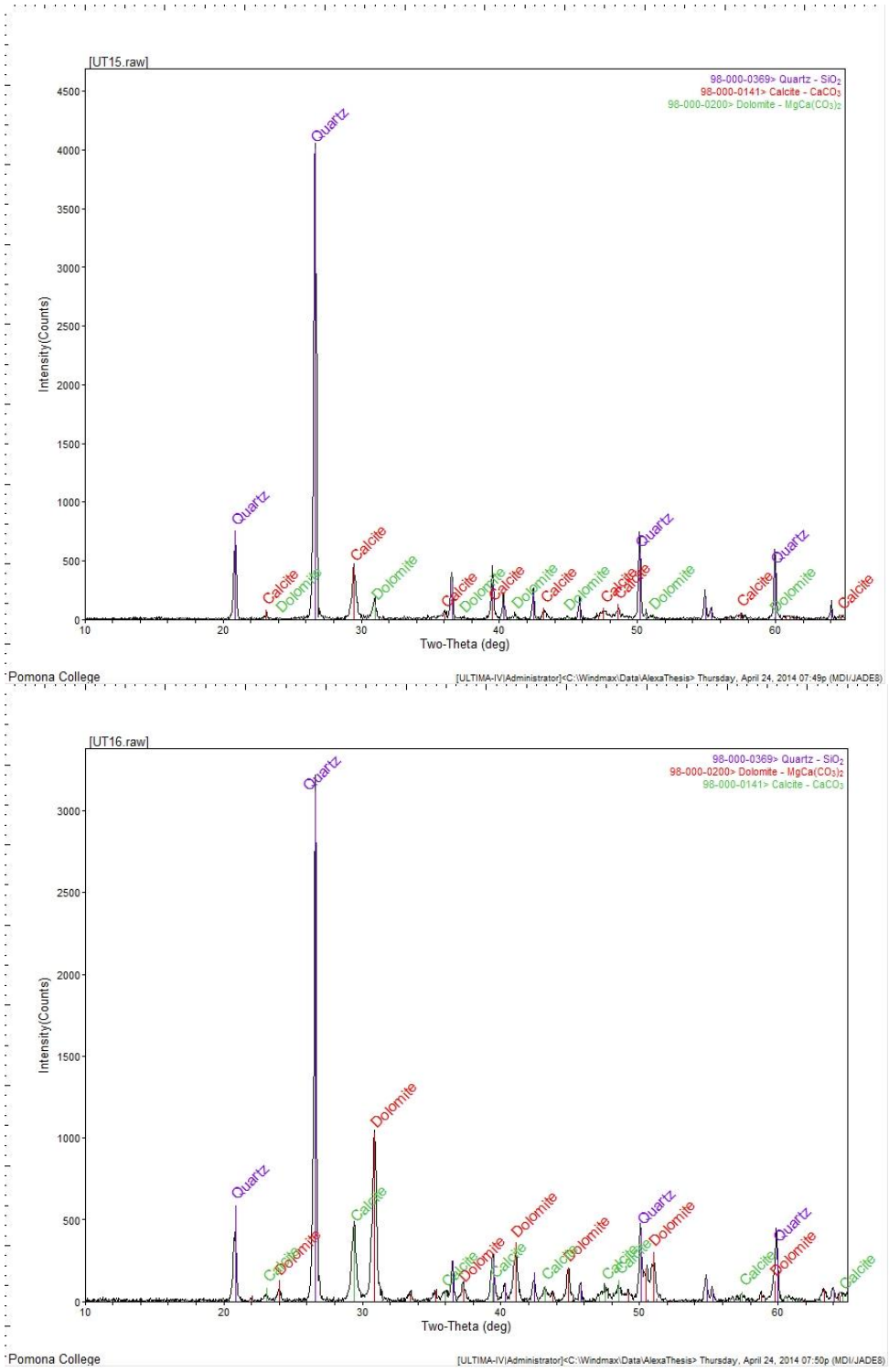

Figure 19: XRD spectra of samples of (A) 13UT-15 from Horse Canyon, and (B) 13UT-16 from Soldier Canyon Mine. Both show quartz, calcite, and dolomite.

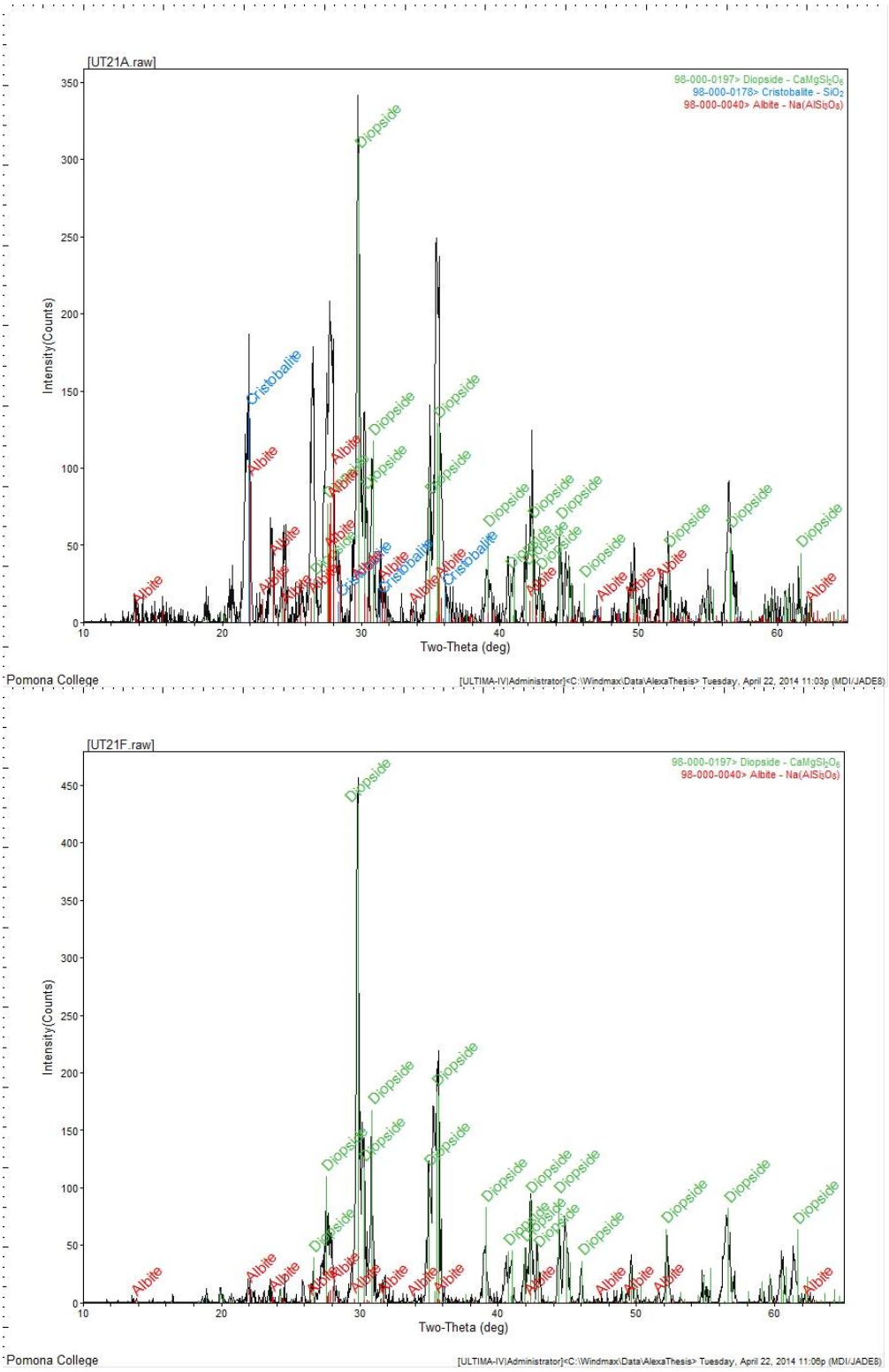

Figure 20: XRD spectra of Helper paralavas. (A) Sample 13UT-21A contains cristobalite, diopside, and albite. (B) Sample 13UT-21F contains diopside and albite.

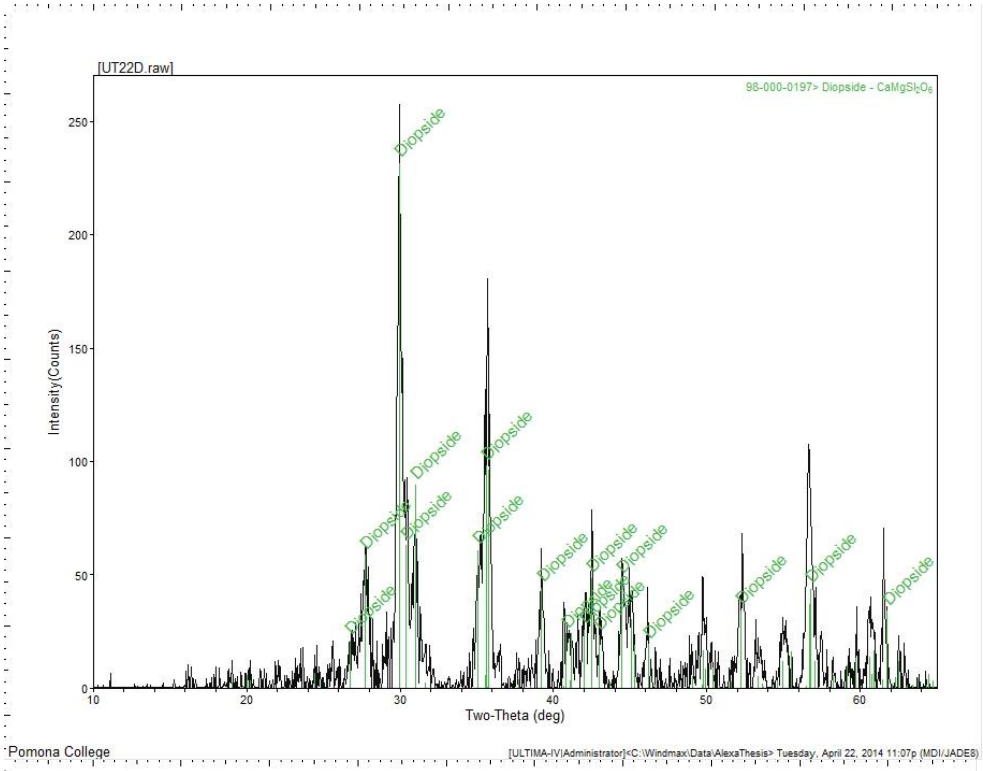

C

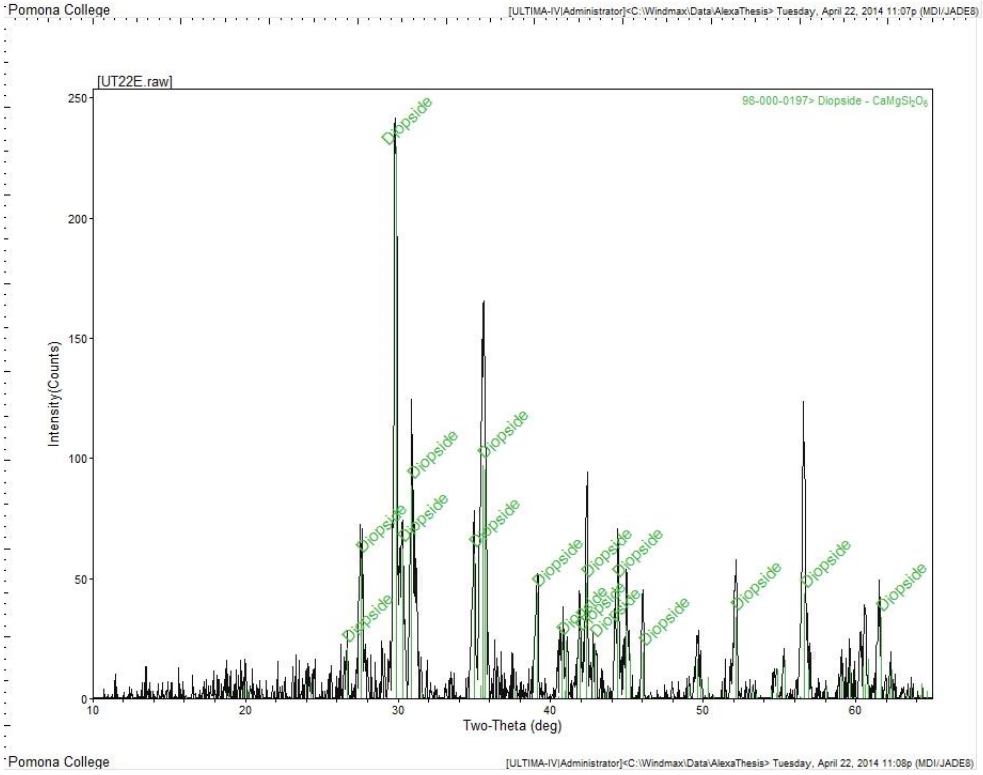

D

Figure 20 (Continued): XRD spectra of Helper paralavas. (C) Sample 13UT-22D is predominately diopside. (D) Sample 13UT-22E contains diopside as well.

The XRD spectra for the vertical transect (Fig. 21) show a variety of high temperature minerals, including cristobalite (SiO_2), tridymite (SiO_2), mullite ($Al_6Si_2O_{13}$), and diopside. Cristobalite appears in the spectra for 13UT-20 and 13UT-21A a green vesiculated paralava. XRD analysis of the Emery samples show that these rocks are typically quartz-rich (Fig. 22).

Petrographic analysis of the Helper samples reveal extraordinary quenched melt textures. Sample 13UT-17 (Fig. 23) appears to have zoned quartz grains bathed in a melt. The high interference colors indicate the presence of calcite. 13UT-22E contains acicular textures within a glassy matrix (Fig. 24). In thin section, the pyroxene bearing melt shows exquisite quench textures in vesicles between melt droplets, showing crystallites oriented at various directions. The long habit and hollowed out cores (hoppered texture) of the pyroxenes demonstrates that this mineral quenched directly from a liquid (Cosca et al., 1989). Most glasses are isotropic in thin section, but show hints of hydration.

SEM and EDS analysis of 13UT-12, a yellow baked sandstone from East Carbon, revealed diopside and hematite rims surrounding quartz grains (Fig. 25). EDS analysis of 13UT-17 (Fig. 26A) displays concentrations of Mg, Ca, and Si. Figure 26B is another SEM image of 13UT-17, with concentrations of Ca, Mg, Fe, and Si. Sample 13UT-20 displayed bright white patches of ilmenite, along with anorthite and cordierite (Fig. 27) In the paralavas, the SEM images of 13UT-22D show diopside grains (confirmed by EDS analysis; Fig. 28), cut in various orientations, thus appearing as rectangles or long spindles. These are again hoppered morphologies with some crystal interiors being melt-filled (Fig. 28B). The random orientation of these crystals again shows no evidence of flow alignment, and thus further evidence of growth in a quenched state from a melt. Crystal rims contain elevated concentrations of Al, whereas the melt cores contain elevated concentrations of K-Ca. There also appear to be dendritic growth of cristobalite, indicated in Figure 28A.

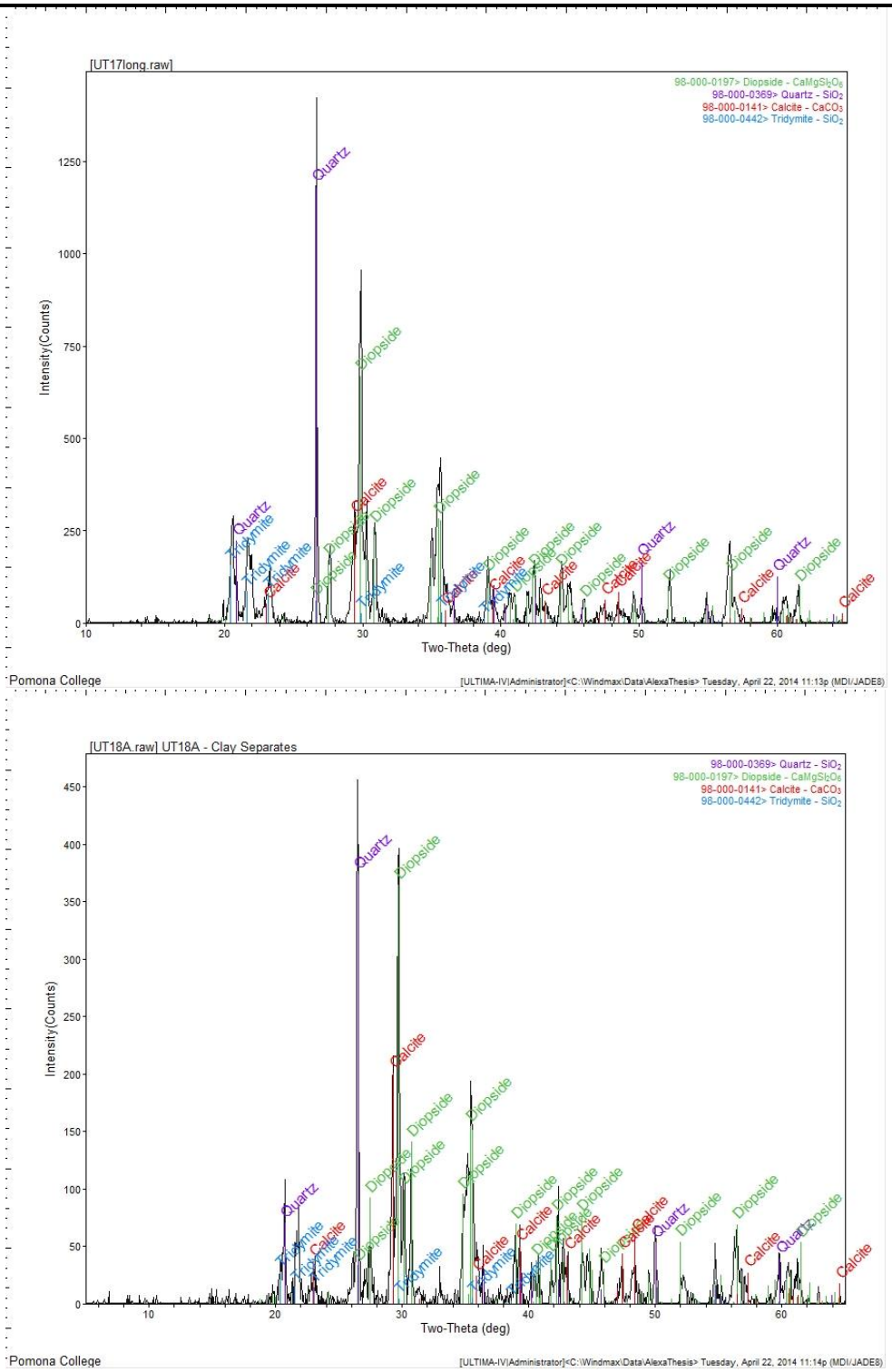

Figure 21: XRD spectra for Helper transect of baked rocks. (A) Sample 13UT-17 at the bottom of the transect, contains high temperature minerals tridymite and diopside. B) Sample UT13-18A contains same minerals 13UT-17.

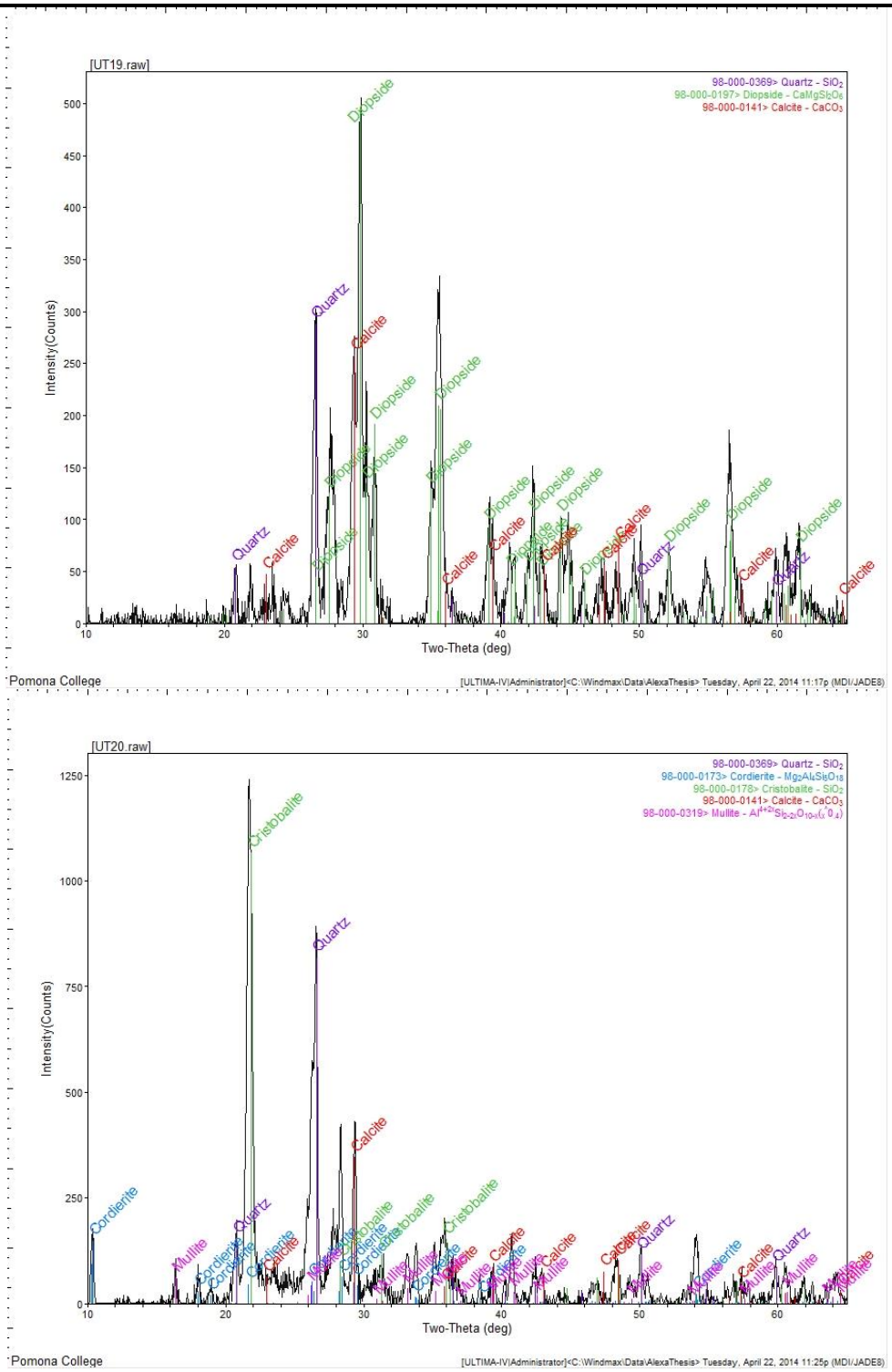

Figure 21 (Continued): (C) Sample 13UT-19 contains diopside, which is intriguing since this sample is not a paralava. (D) Sample 13UT-20 has high temperature minerals cordierite, cristobalite, and mullite.

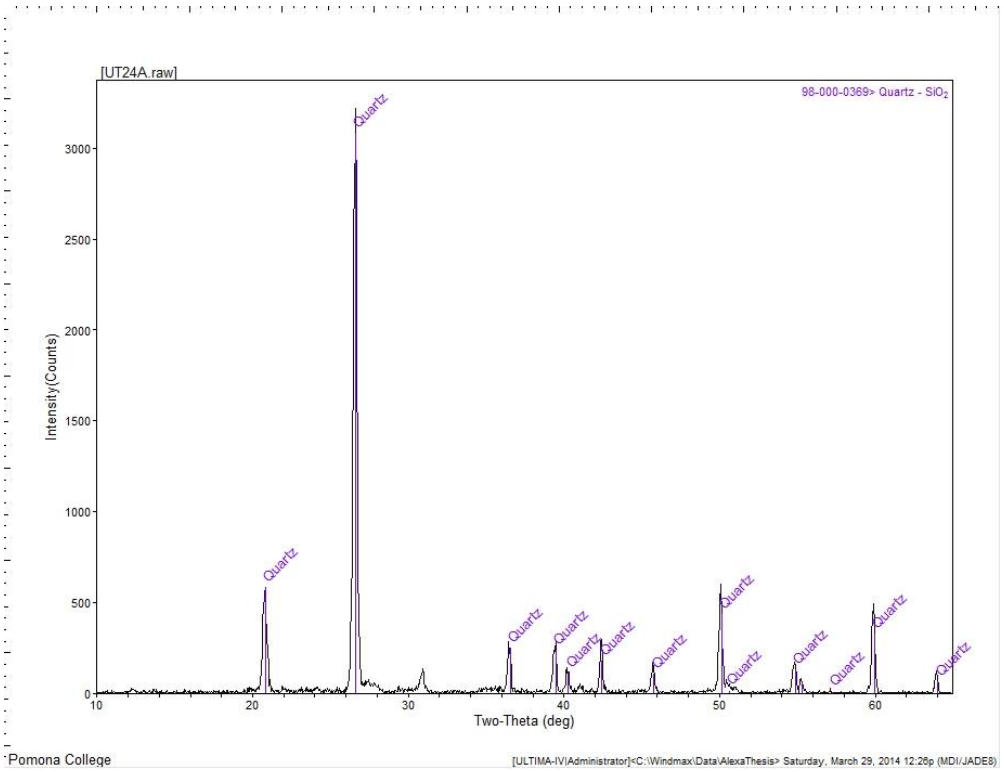

A

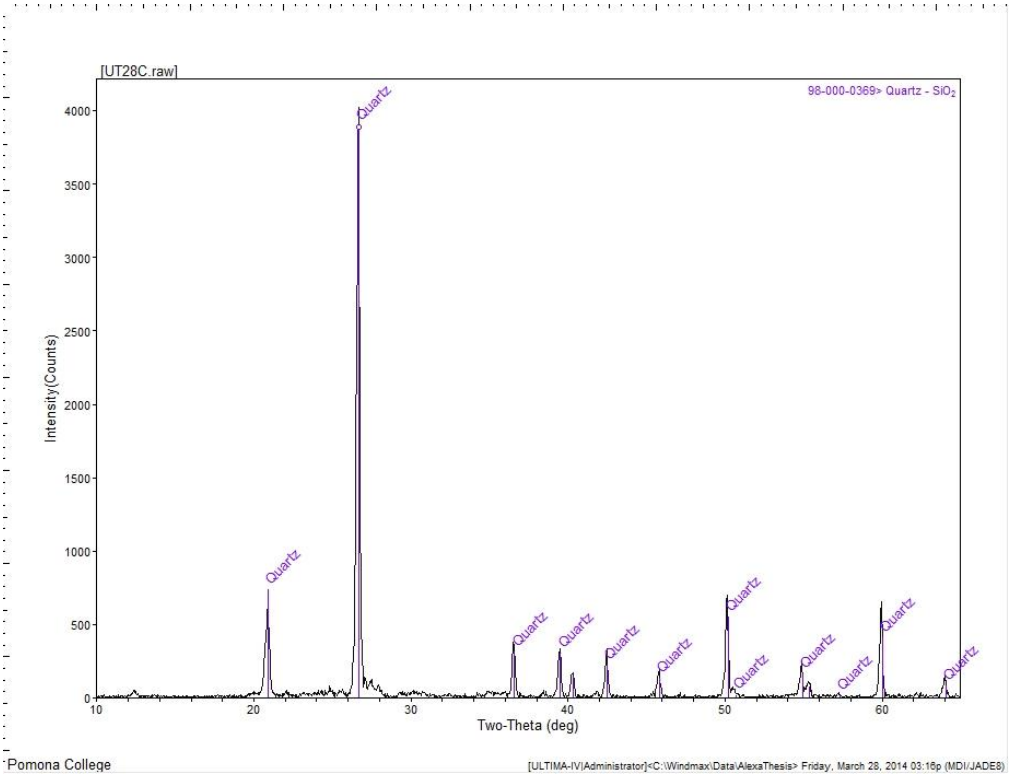

B

Figure 22: XRD spectra of Emery clinker sandstone samples 13UT-24A (A) and 13UT-28C (B). Quartz dominates the overall spectrum for both.

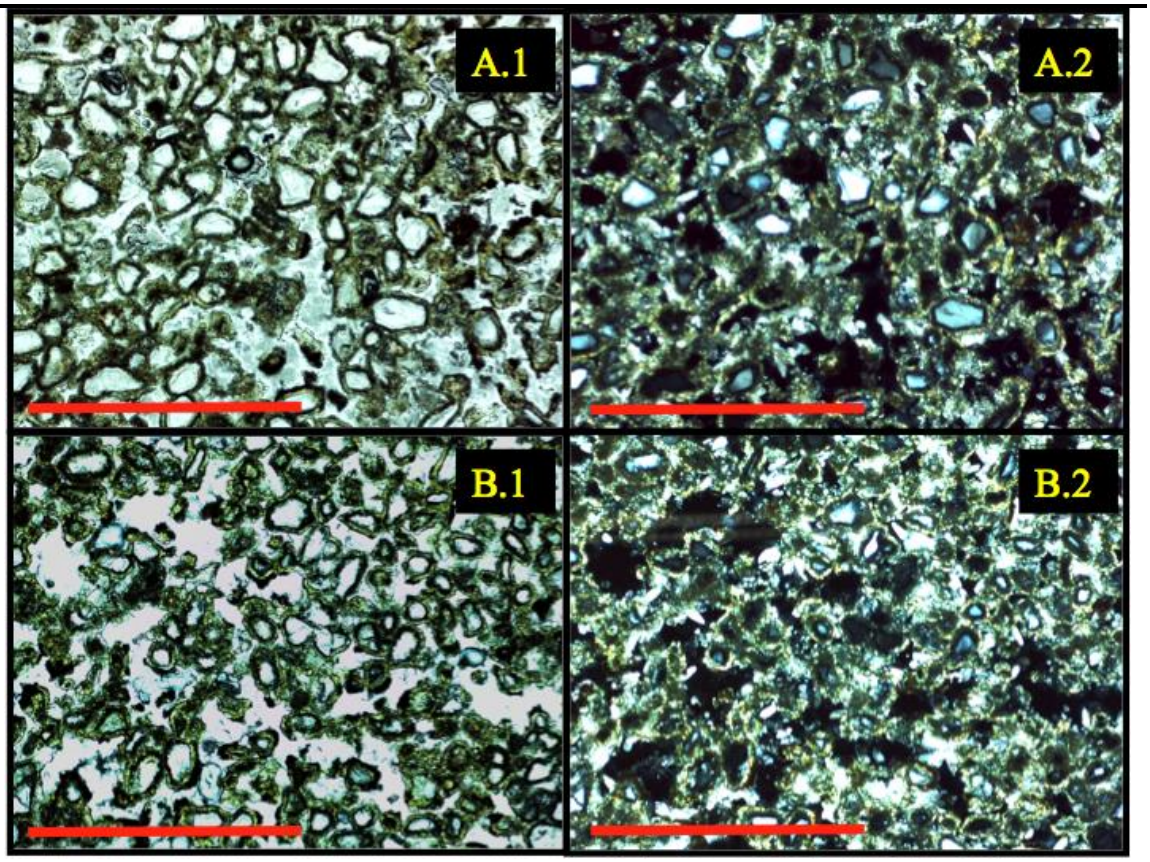

Figure 23: Petrography from 13UT-17. PPL: A.1, B.1; XPL: A.2, B.2. The high inference colors seen in A.2 and B.2 designate calcite, and these grains appear to be surrounded by a diopside melt. Red scale bar is 1 mm in length.

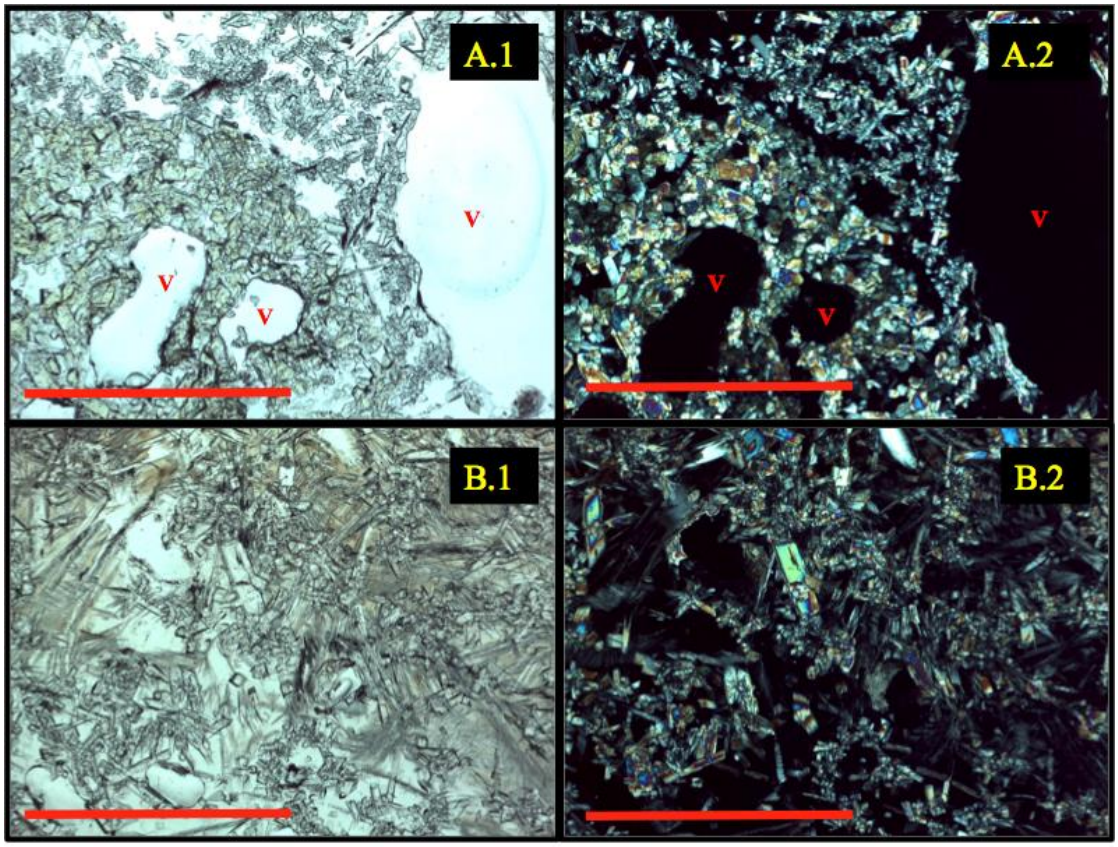

Figure 24: Petrography from 13UT-22E. PPL: A.1, B.1; XPL: A.2, B.2. Vesicles are noted by "V". Acicular textures dominate. Red scale bar is 1 mm in length.

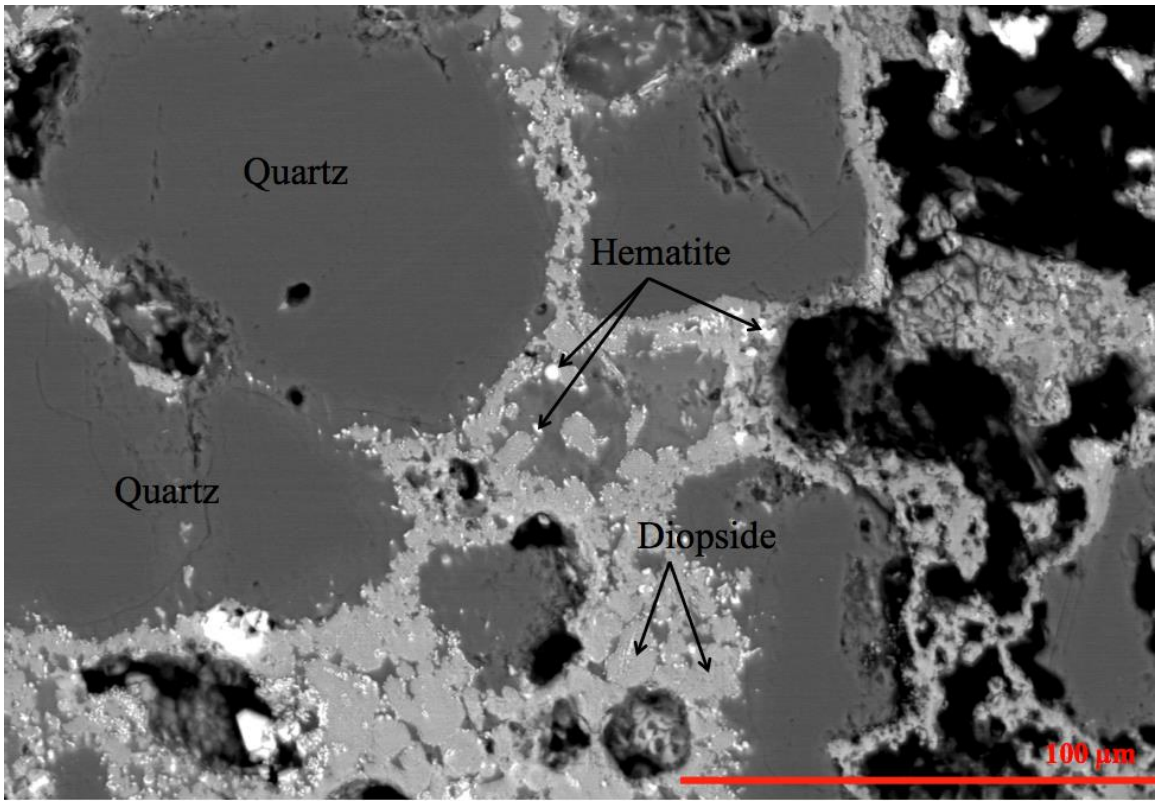

Figure 25: SEM image of East Carbon sample 13UT-12. Diopside and hematite rims surround quartz grains. Fe concentrations revealed by the bright white nodules.

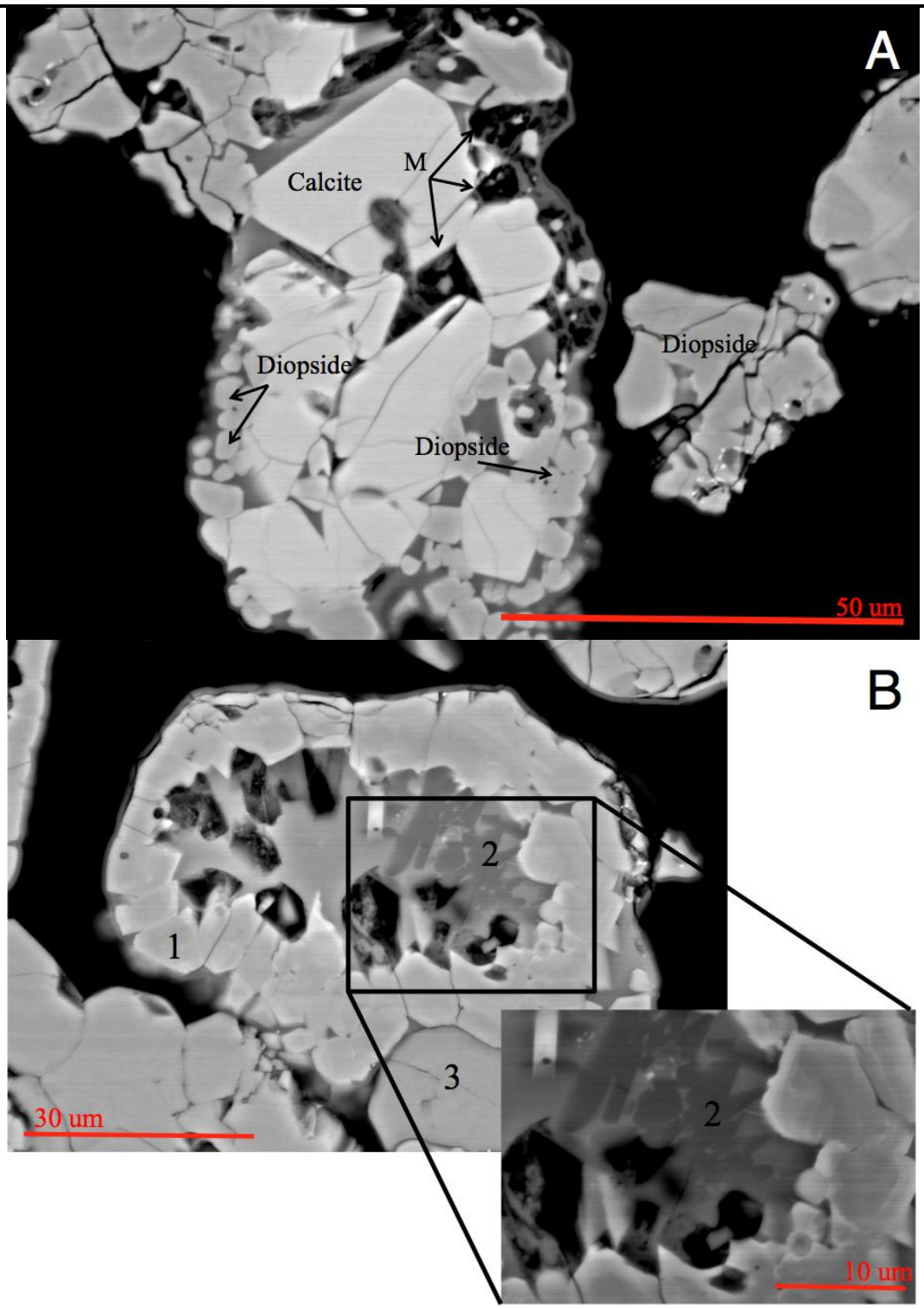

Figure 26: SEM images of 13UT-17. (A) BSE image shows variable greyscales corresponding to different phases in a crystalline melt. Diopside grains surround calcite, with pockets of melt, labeled "M". (B) "The Brain" EDS analysis revealed concentrations of Ca, Mg, Fe, and Si. 1) Diopside rim; 2) Tridymite; 3) Calcite.

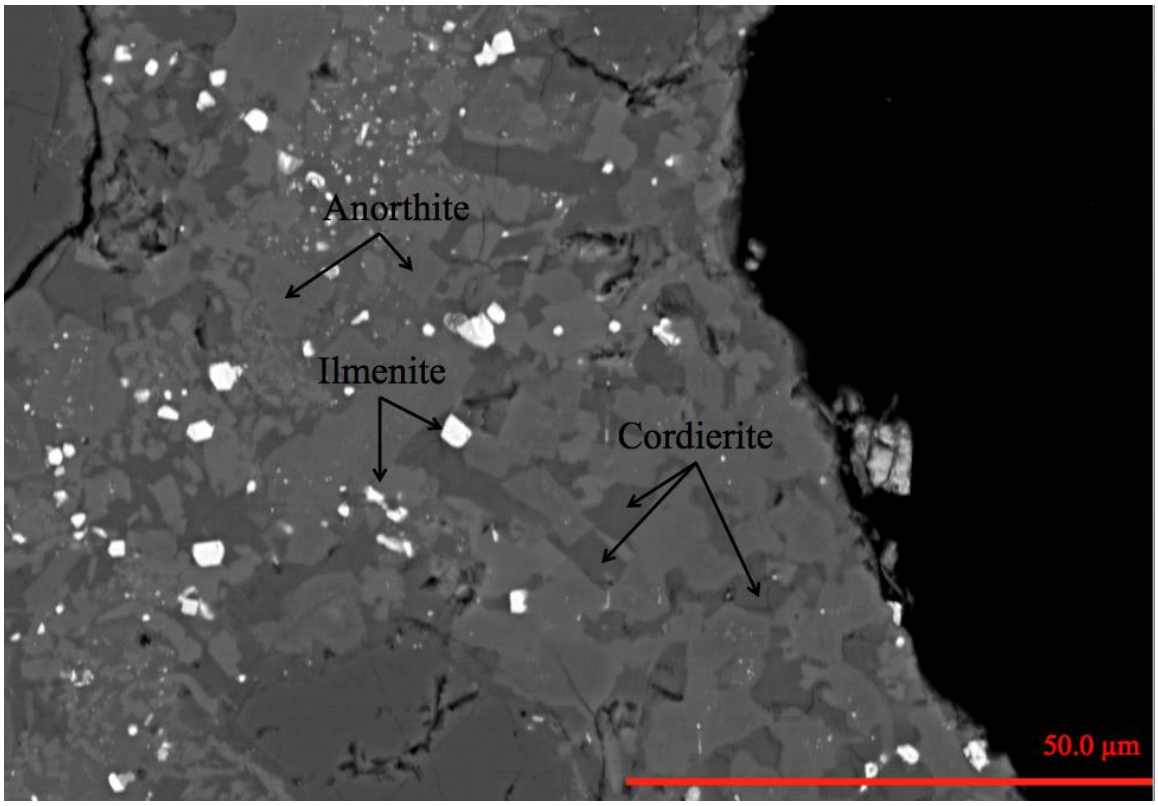

Figure 27: BSE image of Helper sample 13UT-20. Nodules of ilmenite are noted for their bright white color under the SEM. Anorthite grains are present as a light shade of grey, and cordierite is seen as darker grey, rectangular grains.

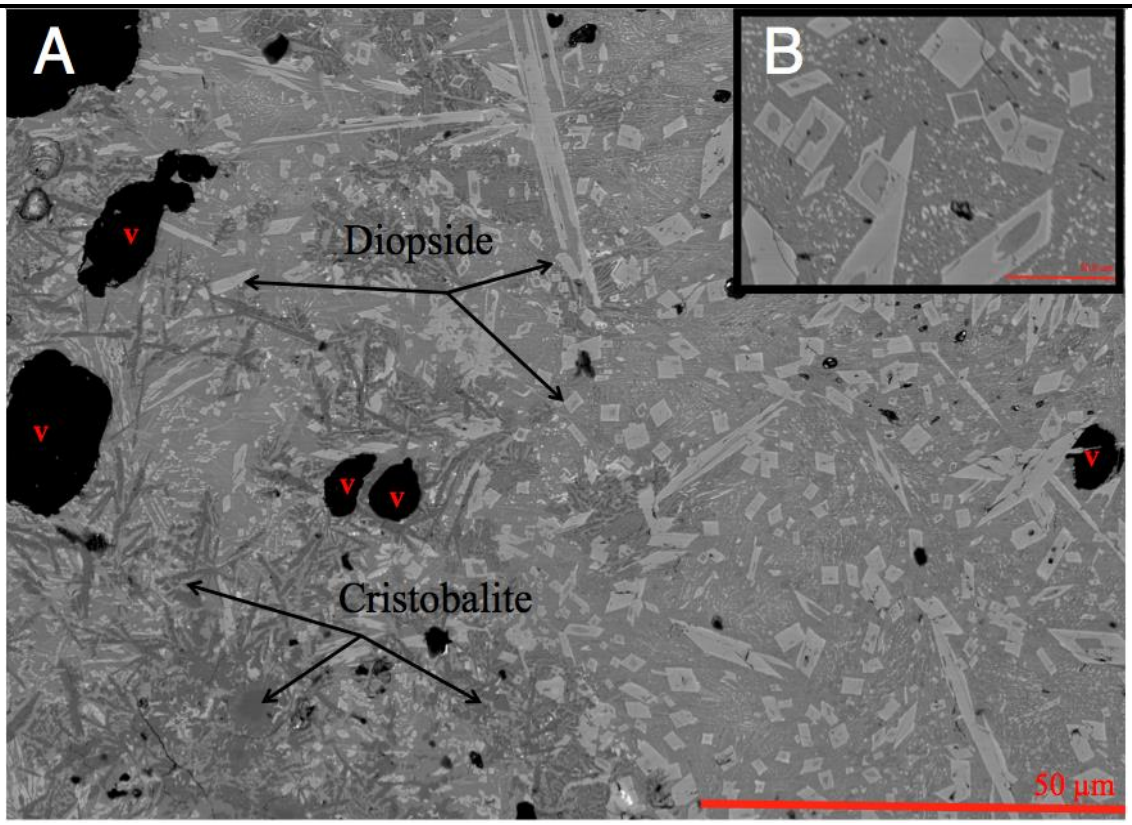

Figure 28: (A) BSE image of paralava sample 12UT-22D from Helper. Diopside grains are shown as rectangles or long spindles, depending on the orientation of the grain when cut. Cristobalite appears in dendritic needles. (B) Closer view of the diopside grains hopper texture.

DISCUSSION

Comparison Between Field Areas

The five field sites are located within two coalfields—Helper and East Carbon are contained within the Book Cliffs coalfields, and the Emery site is within the South Emery coalfield. The Book Cliffs coalfield is contained within the Upper Cretaceous Blackhawk Formation. This coalfield is high-volatile bituminous, with low sulphur, ash, and moisture, and high in heating value (Gloyn et al., 2003). The Emery coalfield is contained within the Upper Cretaceous Ferron Sandstone of the Mancos Shale. Coal quality is high-volatile bituminous. Generally, the Emery coalfield has higher sulfur and ash contents than the Book Cliffs and Wasatch Plateau coalfields (Gloyn et al., 2003). Noted that in the Wasatch Plateau coalfield, the burning of coal beds rarely penetrates farther than 500 ft from the outcrop, and generally no farther than 200–300 ft (Spieker, 1931).

When plotting CaO against SiO_2, the Helper paralavas plot higher in comparison to the Emery and East Carbon samples (Fig. 29). The diopside present in the Helper samples reflects the high CaO and MgO content of the three samples, indicating higher metamorphism temperatures. Phase diagrams describing these elevated temperatures are explained in the next section. Using elevated oxide concentrations as indicators, Helper suggests highest temperatures, with Emery as the lowest, and East Carbon as an intermediate. Figure 29 also plots MgO against SiO_2, with the Helper paralavas trending higher in MgO concentrations compared the other clinker deposits. These plots show the enrichment of Mg and Ca within the melted paralavas compared to other baked clinker deposits.

Peak Temperature

The highest temperature reached within the study area exceeds 1475ºC in the chimney sequences in Helper, determined through comparisons between phase diagrams and observed mineralogy in XRD spectra. High temperature minerals found through XRD analysis in the samples include indialite ($Mg_2Al_4Si_5O_{18}$), augite ($[Si, Al]_2O_6$), tridymite, and cristobalite (Miyashiro et al., 1955). However, indialite and augite have close to exact unit cells to their lower temperature polymorphs of cordierite and diopside, respectively, and therefore, these polymorphs cannot be distinguished from each other, precluding robust temperature estimates based upon the presence of these polymorphs. Thus, indialite and augite were left off of the XRD spectra. However, the potential presence of these minerals merits further discussion. Indialite, the high temperature polymorph of cordierite, forms at 830ºC (Miyashiro et al., 1955). Experiments conducted by

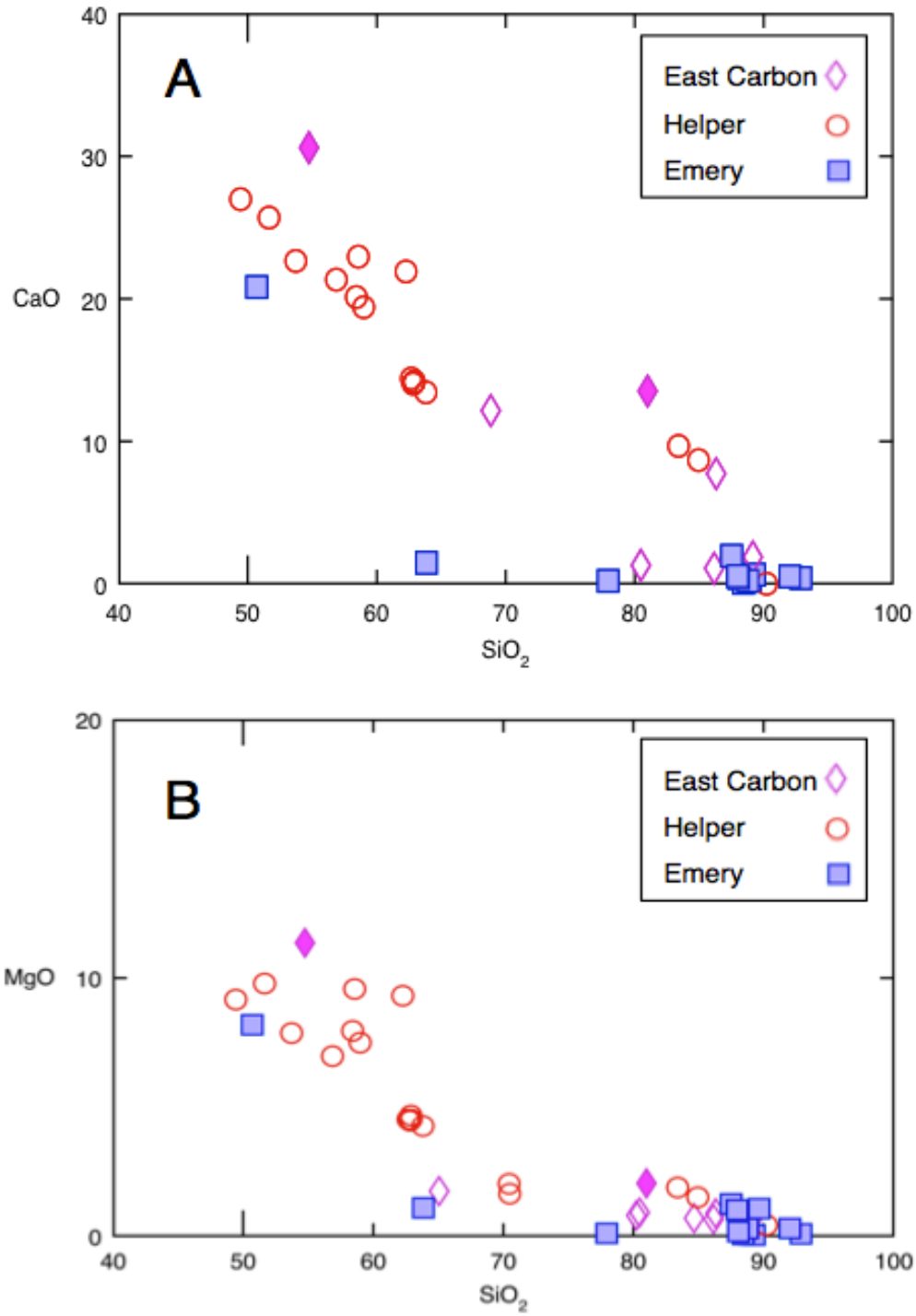

Figure 29: CaO (A) and MgO (B) wt. % for all samples against SiO_2 (wt. %). As Si is depleted, Ca and Mg become enriched, particularly among the Helper samples where diopside is present.

Balassone et al., show volcanically pyrometamorphosed indialite to have a maximum temperature of ~1200ºC (2004). Analysis conducted by Kitamura and Hiroi show that indialite reverts back to cordierite at 700ºC (1982). Cordierite and indialite are contained within sample 13UT-20, which had a small amount of melt. The presence of indialite indicates maximum temperatures between 830-–1200ºC. Augite is the high temperature polymorph of orthopyroxene, and is stable up until about ~1225ºC (Ross and Huebner, 1979). However, since many of the rocks show a good match of diopside and augite, this likely means that there is some solid solution of the clinopyroxene within the samples. Due to the green color of the paralavas, it is more likely to be all diopside with some Fe-substitution. Tridymite, a high temperature polymorph of quartz, appears in Helper samples 13UT-17 and -18. Cristobalite, the highest temperature polymorph of quartz, appears in two Helper samples: 13UT-20 and -21A. Cristobalite reaches a peak temperature of 1723ºC before melting, however this temperature is only reached with pure SiO_2, and temperatures need to be 1723ºC for cristobalite to form (Cosca et al., 1989). Another phase diagram from Dectrov et al., depicts a ternary diagram of SiO_2-CaO-MgO in which diopside is stable between 1331–1392ºC, tridymite from 1338ºC, and cristobalite above 1465ºC. Since cristobalite is present in a couple samples, this indicate that peak metamorphic temperature of the Helper samples exceeded 1465ºC.

The Helper samples contains the assemblage tridymite+diopside, as well as cordierite+mullite+cristobalite. Phase equilibria (Fig. 30) indicate the co-existence of such minerals crystallized from melts at atmospheric pressure. Therefore, sample 13UT-17 and -18, which contain both tridymite and diopside, appear to be a cotectic assemblage that was at least 1369°C. Sample 13UT-20 contains mullite, cordierite, and cristobalite, is an even more restrictive assemblage and suggests minimum temperature exceeding 1465°C, assuming end member compositions.

However there are some limitations in using minerals to correlate peak temperature, most significantly including the prevention of the quartz–tridymite mineral transition. Other sample areas may not be displaying peak temperatures as clearly because of the possibility of local heating and quenching can occur fast enough to prevent the complete transformation of quartz to tridymite or cristobalite, thus not recording the peak temperature in the mineralogy. Additionally, even minor inclusions of other components to the SiO_2 phase may greatly affect the phase diagram (Essene, 1982). Thus, rapid variation in temperature combined with solid solutions may cause metastable development and/or endurance of one or more high temperature polymorphs (Cosca et al., 1989). This rapid variation may cause erroneously high estimates of temperature based solely on the solid phases of melts. Many of the clinker deposits mentioned in Table 4 include a variety of rock types included in the melts and field area overall.

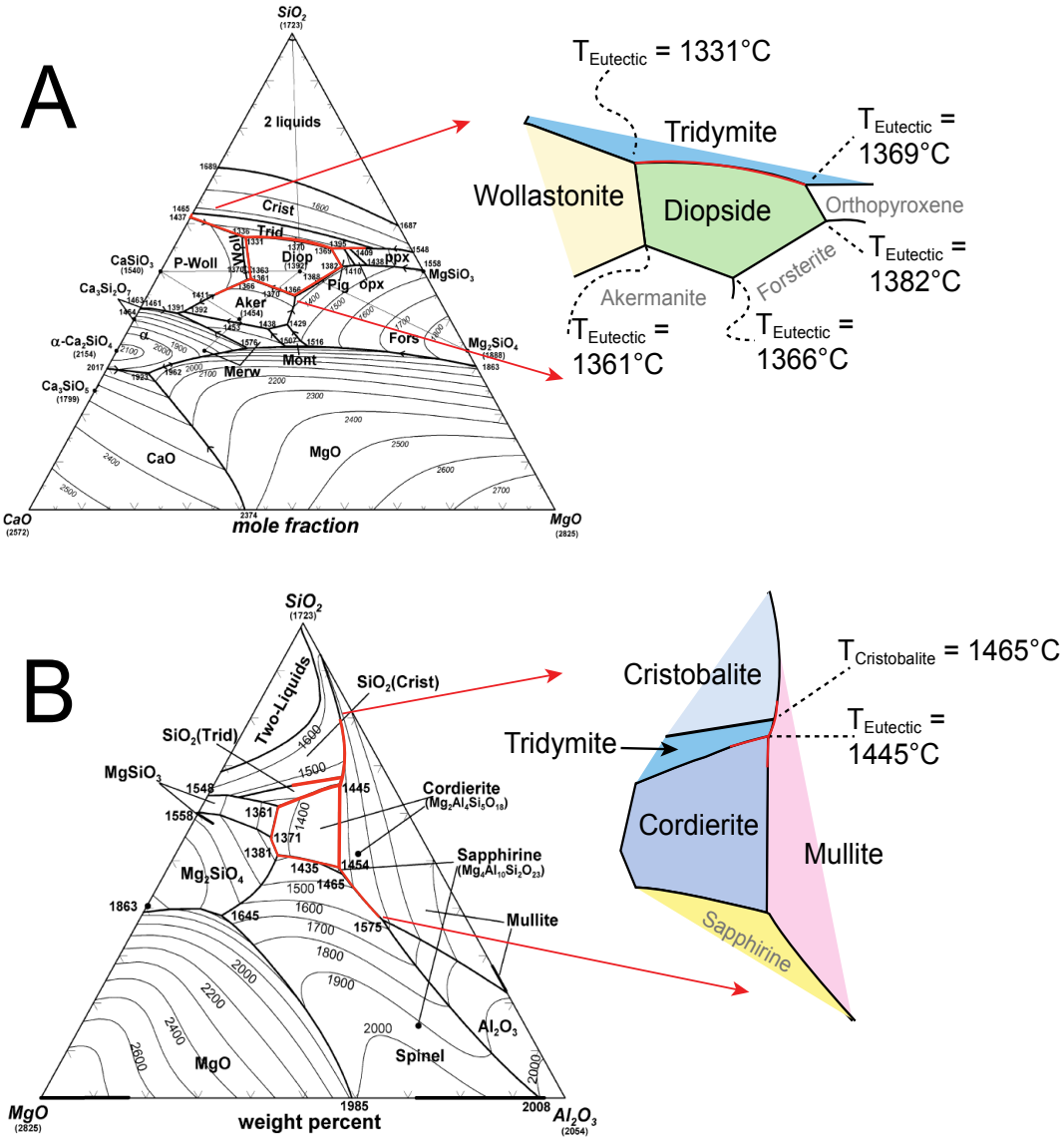

Figure 30: Phase diagrams showing various high temperature assemblages. Red lines highlight assemblages of (A) tridymite+diopside+wollastonite and (B) cristobalite+mullite+cordierite+tridymite, with the latter indicating the highest temperature of 1465ºC. Various eutectics indicate different temperatures. After Dectrov et al., 2009.

TABLE 4: PEAK TEMPERATURES FOR CLINKER LOCATIONS

Peak Temperature (ºC)	Location	Rock Type(s)	Age of Rock	Coal Grade
800–1500[1]	Oslavany, Czech Republic	Coal waste pile/sandstones/ Siltstones/carbonates	Late Carboniferous	Low volatile bituminous to anthracite
1000–1600[2]	Rotowaro, New Zealand	Claystone and unknowns	Eocene	Sub-bituminous
1100[3]	Ricetto, Italy	Sandstone	Late Miocene	N/A
1120–1230[4]	Shanxi Province, China	Siltstone, sandstone, mudstone	Carboniferous–Permian	Bituminous
1146[5]	Sosnowiec, Poland	Sandstones	Carboniferous	N/A
1200[6]	Central Apennines, Italy	Marls, sandstones, siltstones, and claystones	Upper Miocene–Early Pleistocene	Bituminous
1300[7]	Powder River Basin, WY, USA	Shale	Eocene	N/A
>1330	San Rafael Swell, UT, USA	Sandstones, shale	Cretaceous	Bituminous
1400[8]	Kuzbass, Russia	Claystone, siltstone, sandstone	Middle Carboniferous–Lower Permian	N/A

[1] Dokoupilová, et al., 2007; [2] Masalehdani, et al., 2007; [3] Capitanio, et al., 2004; [4] Grapes, et al., 2009; [5] Gaweda, et al., 2013; [6] Melluso, et al., 2003; [7] Cosca, et al., 1989; [8] Novikova, 2009

Studies from around the world have shown a variety of peak temperatures associated with pyrometamorphic deposits, with some possibly reaching 1600ºC (Masalehdani et al., 2007). In Italy, the pyrometamorphism of sandstone reached 1100ºC when melilite crystallization conditions were reached (Capitanio et al., 2004). Another Italian location of shale and marl recorded a minimum liquidus temperature at 1200ºC (Melluso et al., 2003). In Russia, baked claystone, siltstone and sandstone reached 1400ºC (Novikova, 2009). Moving farther east, Grapes et al. found peak temperatures of paralavas resulting from siltstone, mudstone, and sandstone to be 1120–1230ºC (2009). New Zealand also has clinker deposits, with temperatures reaching 1600ºC (Masalehdani et al., 2007). In the United States, clinker deposits in the Powder River Basin, WY reached maximum temperatures of 1300ºC (Cosca et al., 1989; Clark and Peacor, 1992). Paralavas and clinker deposits do not only form from coal seam fires, but also from coalmine waste dumps. Temperatures reached up to 1146ºC for paralavas from a coalmine waste dump fire in Poland (Gaweda et al., 2013). In the Czech Republic, another coalmine waste pile fire recorded temperatures from 800–1500ºC (Dokoupilová et al., 2007). A summary of these results can be found in Table 4. Peak temperatures describing in this study are comparable to the work of others.

Controls on Peak Temperature

The Helper outcrop displays maximum metamorphism and temperature within the study area, perhaps because of the structure of the area itself. In Figures 11 and 12, the bedding of the outcrop appears to be curved into an antiform. No other outcrop in the field areas displayed such curvature. This additional metamorphism may have affected the coal by compressing it or altering it further, permitting ultra-hot combustion. Tectonic and structural activity could increase the porosity of the coal seams and host rock, allowing for higher oxidation (Quintero et al., 2009). However, the area is not particularly active tectonically. The coal seam is not visible, but it may be a thick seam, allowing for a longer, hotter, continued burn. It is also interesting that this antiform has not collapsed in, as it is assumed that there is a significant amount of vacated area below the outcrop where the coal burned away. Intriguingly, the chimney system appears intact, as cool air was felt venting out of the chimney structures during field examinations.

The rank and composition of coal may have had the largest effect on pyrometamorphic temperature. Lignites and sub-bituminous coals can spontaneously combust at 300ºC, and bituminous coal can spontaneously combust only when it reaches 500ºC (Quintero et al., 2009). However, lower coal ranks may favor spontaneous combustion because of the higher porosity, volatile matter, and moisture content (Misra and Singh, 1994). Sub-bituminous coals have higher concentrations of reactive macerals (organics), which increases the propensity toward temperature

elevation (Quintero et al., 2009). The presence of pyrite in the coal may also act as a catalyst for oxidation reactions (Carras and Young, 1994). Moreover, at elevated humidity, pyrite experiences exothermal oxidation, in turn expediting coal self-heating (Banerjee, 1985). In addition, the presence of siderite (Misra and Singh, 1994) and calcite (Sujanti and Zhang, 1999) can also promote spontaneous combustion.

Although the coal in the study area is bituminous and thus needs higher temperatures to spontaneously combust, there is a significant amount of coal visible at the surface. This visible coal can degrade and oxidize, thus increasing porosity and access to meteorological moisture, which in turn increases susceptibility for spontaneous combustion. The active mining in the area also increases risk, opening vents for oxidation and drying out when exposed to the atmosphere.

Bulk Metal Re-distribution

Overall, pyrometamorphism of the field sites does not appear to have significant effects on heavy metal mobility. There were no discernible trends from the XRF data when comparing unaltered vs. altered sandstones. However, analysis of the paralavas indicates possible metal mobility. Figure 31 demonstrates the separation of clinker rock from paralavas in terms of metal content, indicating a shift in concentration. These paralavas came directly from the clinker deposits, and the only cause of compositional change is heat. The clinker deposits are condensing in volume, and thus concentrating in the metals present, creating a type of slag. Thus, temperatures must be extremely high in order to mobilize the metals. Since the paralavas contain diopside, and this phase forms at 1361°C, metal mobility may begin around this temperature (Figure 30).

Further investigation of the Helper samples reveals convincing evidence for metal mobility. Figure 32 depicts plots of Cr, Zn, V, and CaO/MgO ratio against TiO_2. Figure 32A shows the paralavas as an intermediate between various clinker samples, possibly signifying a bulk mixing line. Zn concentrations are higher in the melts, though some protoliths are also enriched (Fig. 32B). Despite TiO_2 being greater in the melts overall, there is a strong trend with V increasing as well. Clusters of melts indicate different melt type compositions (Fig. 32C). For the CaO/MgO ratio, the values vary throughout the protoliths, but the melts are distinctly grouped. However, sample 13UT-21F is anomalous. These enriched metal concentrations may leach out into the surrounding area.

Additionally, the burning of coal seams could simulate fly ash. Fly ash is the particulate material produced from the combustion of coal in power plants (Cho et al., 2005). Fly ash can reemit metals back into the environment directly through contact where they are stored (Soco and Kalembkiewicz, 2007), or through atmospheric emission via stack (Fernandez-Turiel et al., 1994). Through laboratory analysis, Soco and Kalembkiewicz found that 2.6% of Cu and 3.4% of Zn of

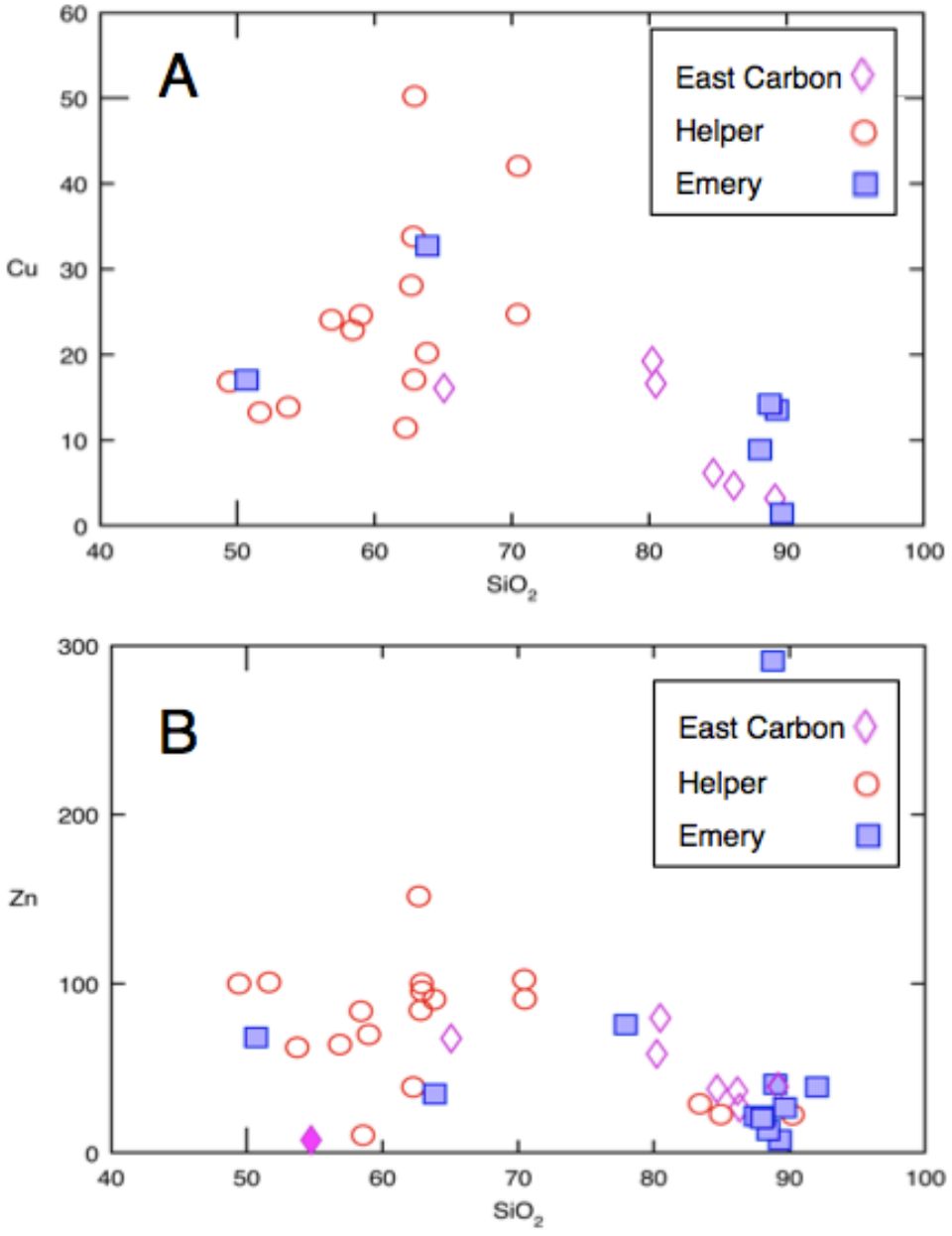

Figure 31: Metal concentrations (ppm) of all samples vs. SiO_2 (wt. %). (A) For Cu, there is a low vs. high Si break, with the Helper samples containing lower Si, and Emery and East Carbon having higher Si content. The hotter Helper samples also have higher Cu concentrations. (B) Slightly higher Zn concentrations for Helper samples.

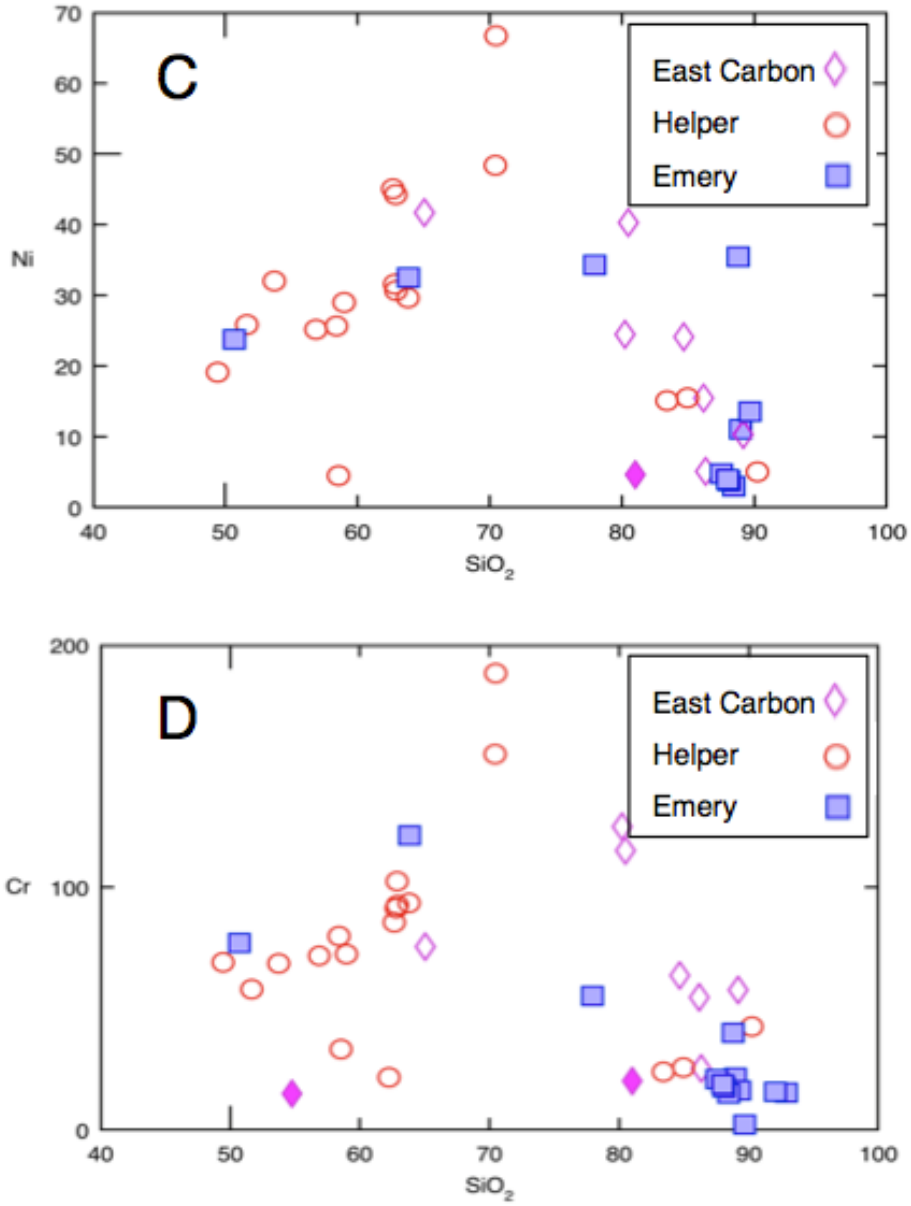

Figure 31 (Continued): (C) Ni concentrations to not have a strong correlation; (D) Emery samples appear fairly homogenous for Cr content, concentrating around the 90% SiO_2 mark.

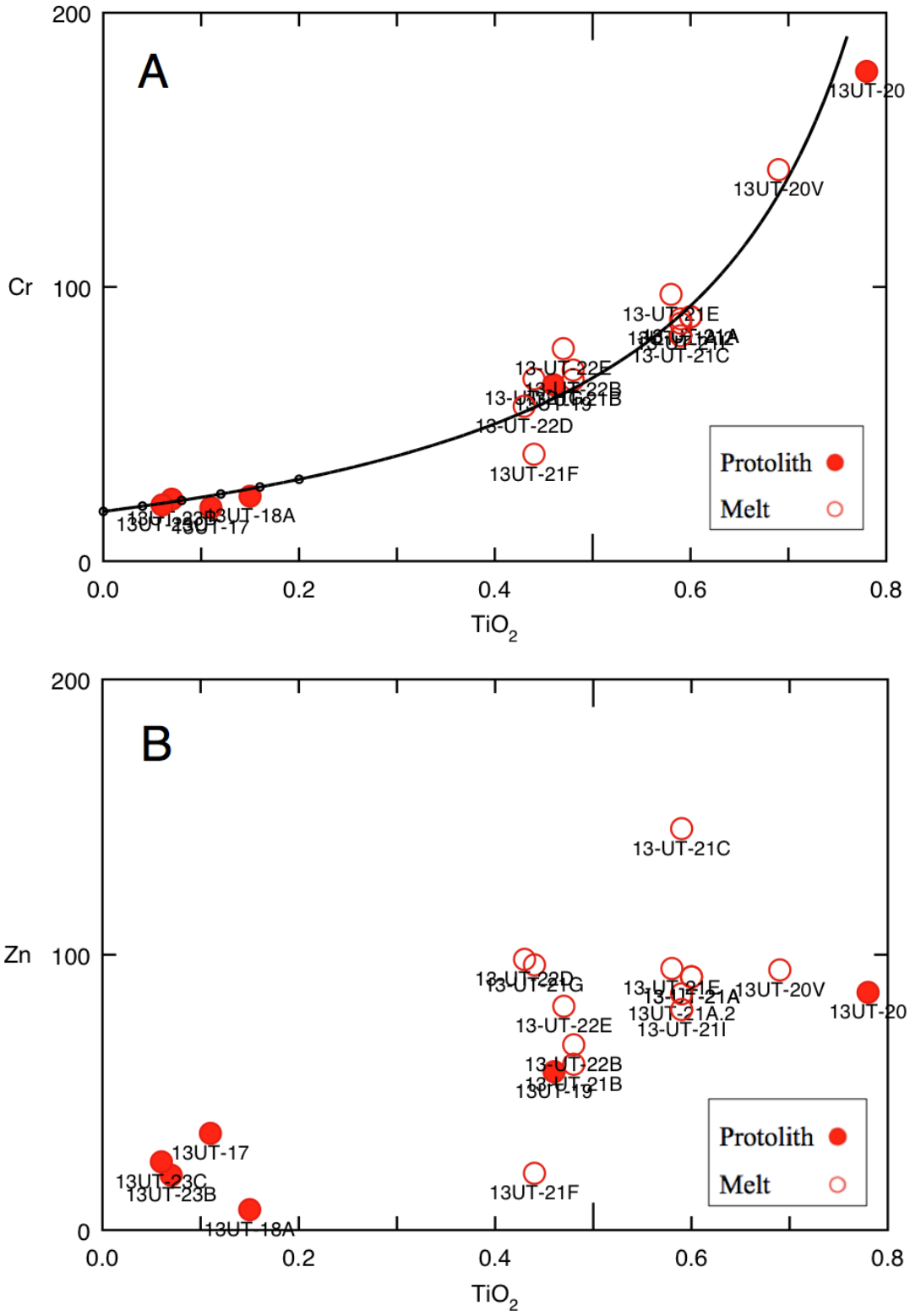

Figure 32: Helper protolith and melt sample show distinctions in metal mobility. (A) Cr presents a possible bulk mixing line, with two melt populations between two protolith groups. (B) Discrete separation between melth and protolith for Zn cocentrations.

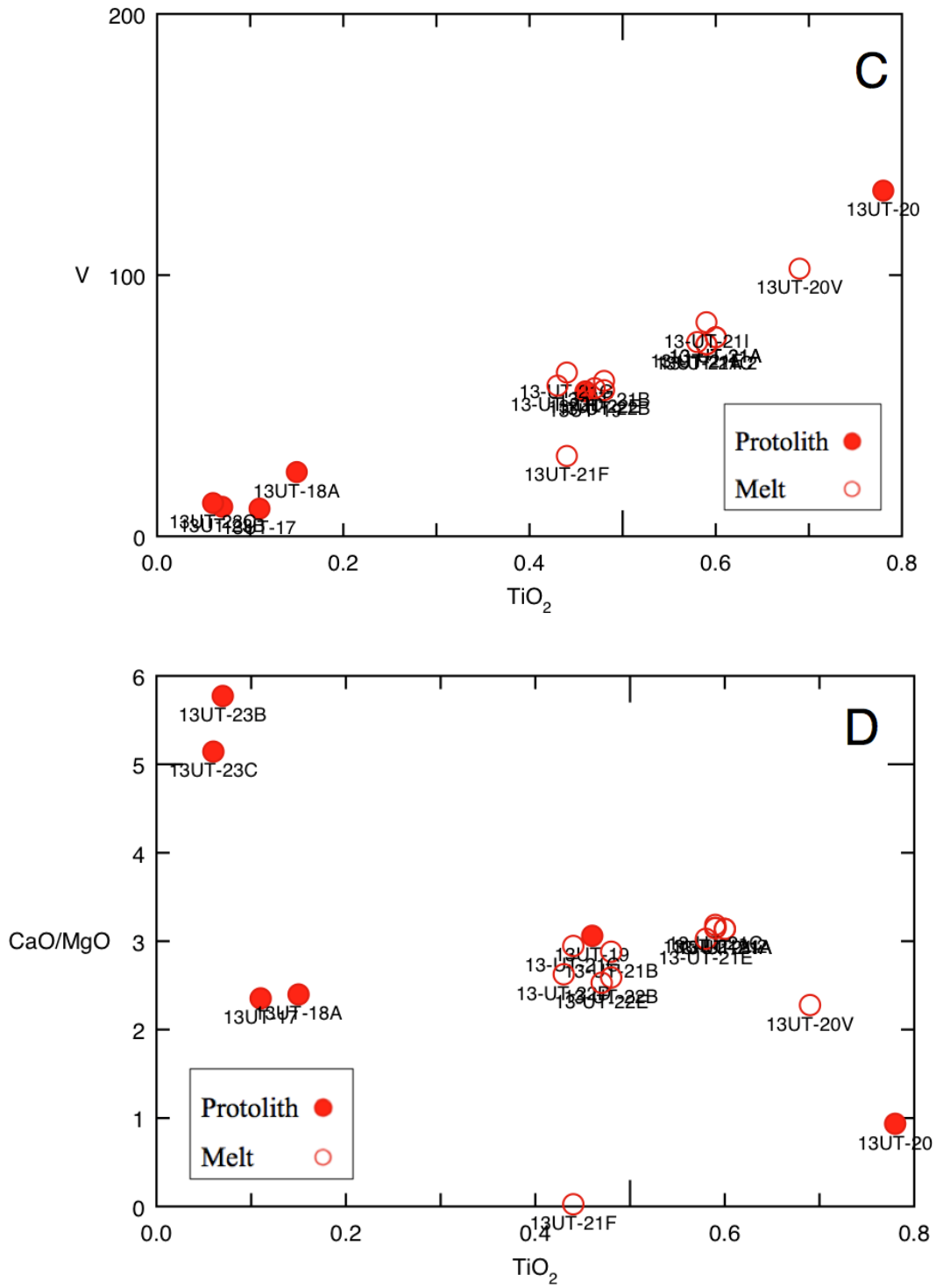

Figure 32 (Continued): (C) Distinct grouping of paralavas. As TiO_2 increases in concentration, V becomes enriched as well. (D) Though the protoliths show no trends, the paralavas are again in two distinct groups for CaO/MgO. However, sample 13UT-21F is anomalous.

their original concentrations in the fly ash can be leached into the environment (2007). Fernandez-Turiel et al., conducted experiments on the metal mobility of Cd, Co, Cu, Ni, Pb, Sb, and Zn within fly ash (1994). Their results showed higher percentages of extractable fractions, with percentages of up to 16.8 (Cd), 16.6 (Co), 10.8 (Cu), 4.2 (Ni), 0.6 (Pb), 18.9 (Zn). Cadmium is the most water-extractable, whereas cobalt shows low solubility. These percentages are high, and thus have high leaching potential. Cadmium would have the highest potential if the fly ash is stored in ponds or landfills because of water content.

Baked clinker deposits themselves may not pose an increased health risk, but coal fires are an active, ongoing hazard as these fly ash experiments show. The gases coming out of a chimney sequence during active combustion may be toxic and vary in composition as temperatures elevate. In medium-volatile bituminous coal, temperatures for gas release include 110ºC for carbon monoxide (CO), 170ºC for hydrogen (H_2), 240ºC for hydrocarbons ethylene (C_2H_4), and 300ºC for propylene (C_2H_6) (Stracher and Taylor, 2004). These gases can cause asphyxiation at high concentrations. Since coal fires are actively burning in the Emery coalfield, they are likely releasing these hazardous gases.

CONCLUSION

The coalfields surrounding the San Rafael Swell are an important economic resource for Utah, but also pose elevated risk for coal fires because of the amount of coal exposed to atmospheric conditions caused by mining activity. The Helper, UT samples indicate phase equilibria of assemblages of diopside+tridymite and codierite+cristobalite+mullite, which show eutectic temperatures ranging from 1369–1465°C. Though the process of pyrometamorphism does not increase metal mobility in baked clinker deposits, there is evidence of mobility within the paralavas, posing a risk for metals leaching into the environment.

ACKNOWLEDGEMENTS

Sincere thanks must be given to Professor Jade Star Lackey for his enthusiasm, expertise, and encouragement. Thank you to Professor Bob Gaines for his insightful observations and recommendations. This process was made significantly better because of the cheer, helpfulness, and optimism of Jonathan Harris and Lori Keala. Juliet Ryan-Davis was instrumental in working the SEM, making a beautiful epoxy billet, and providing reassurance. Funding provided by the Pomona College Dean's Office. Finally, I wish to thank my peers and friends within the department; I do not know how I would have gotten through it all without your humor and support.

REFRENCES CITED

Annual Coal Report, 2012**,** United States Energy Information Administration, http://www.eia.gov/coal/annual/pdf/acr.pdf (accessed March, 2014).

Balassone, G., Franco, E., Mattia, C. A., and Puliti, R., 2004, Indialite in xenolithic rocks from Somma-Vesuvius (Southern Italy): Crystal chemistry and petrogenic features: American Mineralogist, v. 89, p. 1–6.

Banerjee, S. C., 1985, Spontaneous Combustion of Coal and Mine Fire. Oxford and IBH Publishing Company, New Delhi.

Bluemle, J., 2005, North Dakota Notes no. 13, North Dakota's Clinker: https://www.dmr.nd.gov/ndgs/ndnotes/ndn13_h.htm (accessed November 2013).

Boden, T., Vanden Berg, M., Krahulec, K., Tabet, D., and Gwynn, M., 2011, Utah's Extractive Resource Industries 2011: Utah Geological Society, Circular 115.

Capitanio, F., Larocca, F., and Improta, S., 2004, High-temperature rapid pyrometamorphism induced by a charcoal pit burning: The case of Ricetto, central Italy: International Journal of Earth Science, v. 93, p. 107–118.

Carras, J. N., and Young, B. C., 1994, Self-heating of coal and related materials: Models, application and test methods: Progress in Energy and Combustion Science, v. 20, p. 1–15.

Cho, H., Oh, D., and Kim, K., 2005, A study on removal characteristics of heavy metals from aqueous solution by fly ash: Journal of Hazardous Materials, v. B127, p. 187–195.

Clark, B. H., and Peacor, D.R., 1992, Pyrometamorphism and partial melting of shales during combustion metamorphism: mineralogical, textural, and chemical effects: Contributions in Mineralogy and Petrology, v. 112, p. 558–568.

Cosca, M., Essene, E., Geissman, J., Simmons, W., and Coates, D., 1989, Pyrometamorphic rocks associated with naturally burned coal beds, Powder River Basin, Wyoming: American Mineralogist, v. 74, p. 85–100.

Davis, G., and Bump, A., 2009, Structural geologic evolution of the Colorado Plateau: Geological Society of America Memoir 204, p. 99–124.

De Boer, C., Dekkers, M., and Van Hoof, T., 2001, Rock-magnetic properties of TRM carrying baked and molten rocks straddling burnt coal seams: Physics of the earth and planetary interiors, v. 126, p. 93–108.

Dokoupilová, P., Sracek, O., and Losos, Z., 2007, Geochemical behavior and mineralogical transformations during spontaneous combustion of a coal waste pile in Olsavany, Czech Republic: Mineralogical Magazine, v. 71(4), p. 443–460.

Essene, E. J., 1982, Geologic thermometry and barometry: Mineralogical Society of America Reviews in Mineralogy, v. 10, p. 153–206.

Fernande-Turiel, J. L., de Carvalho, W., Cabañas, M., Querol, X., and López-Soler, A., 1994, Mobility of heavy metals from coal fly ash: Environmental Geology, v. 23, p. 264–270.

Foit, F., Hooper, R., and Rosenberg, P., 1987, An unusual pyroxene, melilite, and iron oxide mineral assemblage in a coal-fire buchite from Buffalo, Wyoming: American Mineralogist, v. 72, p. 137–147.

Gaweda, A., Janeczek, J., Kierepka, M., Kadziolko-Gawel, M., and Krzykawski, T., 2013, Indialite-rich paralava from a coalmine waste-dump, Sosnowiec, Poland: Neues Jahrbuch fur Mineralogie-Abhandlugen, v. 190 (3), p. 237–251.

Geissinger, J., 1990, Managing underground mine fires: the case of Centralia, Pennsylvania: The Pennsylvania Geographer, v. 28 (2), p. 22–26.

Gloyn, R.W., Tabet, D.E., Tripp, B.T., Bishop, C. E., Morgan, C.D., Gwynn, J.W., and Blackett, R. E., 2003, Energy, mineral, and ground-water resources of Carbon and Emery Counties, Utah: Utah Geological Survey, Bulletin 132.

Grapes, R., Zhang, K., and Peng, Z., 2009, Paralava and clinker products of coal combustion, Yellow River, Shanxi Province, China: Lithos, v. 113, p. 831–843.

Heffern, E., and Coates, D., 2004, Geologic history of natural coal-bed fires, Powder River Basin, USA: International Journal of Coal Geology, v. 59, p. 25–47.

Johnson, D. M., Hooper, P. R., and Conrey, R. M., 1999, XRF Analysis of Rocks and Minerals for Major and Trace Elements on a Single Low Dilution Li-tetraborate Fused Bead: Advances in X-ray Analysis v. 41, p. 843–867

Kitamura, M., and Hiroi, Y., 1982, Indialite from Unazuki pelitic schist, Japan, and its transition texture to cordierite: Contributions to Mineralogy and Petrology, v. 80, p. 110–116.

Lackey, J.S., Robinson, C., Windham, C., Frazer, R., and Bindeman, I., 2012, The Fine Gold Intrusive Suite: The Roles of Basement Terranes and Magma Source Development in the Early Cretaceous Sierra Nevada Batholith: Geosphere, v. 8, p. 292–313.

Lindqvist, J., Hatherton, T., and Mumme, T., 1983, Magnetics anomalies above burnt coal seams have potential application in exploration of central Otago and Southland lignite deposits: New Zealand Geological Survey, N.Z.G.S. Report M, p. 1–16.

Lyman, R., and Volkmer, J., 2001, Pyrophoricity (spontaneous combustion) of Powder River basin coals – considerations for coalbed methane development; Wyoming State Geological Survey, Coal Report CR-01-1.

Masalehdani, M., Black, P., and Kobe, H, 2007, Mineralogy and petrography of iron-rich slags and paralavas formed by spontaneous coal combustion, Rotowaro coal field, North Island, New Zealand: Reviews in Engineering Geology, v. 18, p. 117–131.

Meij, R., and te Winkel, H., 2007, The emissions of heavy metals and persistent organic pollutants from modern coal-fired power stations: Atmospheric Environment, v. 41, p. 9262–9272.

Memmi, J., 2000, Cooking Centralia: a recipe for disaster: Geotimes, v. 45 (9), p. 26–27.

Melluso, L., Conticelli, S., D'Antonio, M., Mirco, N., and Saccani, E., 2003, Petrology and mineralogy of wollastonite-and melilite-bearing paralavas from the Central Apennies, Italy: American Mineralogist, v. 88, p. 1287–1299.

Mining Safety and Health Administration (MSHA), Genwal Resources Inc., Crandall Canyon Mine, Mine ID: 4201715: http://www.msha.gov/Genwal/CrandallCanyon.asp (accessed November, 2013).

Misra, B.K, and Singh, B. D., 1994, Susceptibility to spontaneous combustion of Indian coal and lignite: an organic petrographic autopsy: International Journal of Coal Geology, v. 25, p. 265–286.

Miyashiro, A., Iiyama, T., Yamaski, M., and Miyashiro, T., 1955, The Polymorphism of Cordierite and Indialite: American Journal of Science, v. 253, p. 185–208.

Novikova, S. A., 2009, Fayalite from Fe-rich paralavas of ancient coal fires in the Kuzbass, Russia: Geology of Ore Deposits, v. 58(8), p. 800–811.

Quick, J., 2005, Mercury in Coal, Utah Geological Society: http://geology.utah.gov/emp/mercury/index.htm (accessed November 2013).

Quintero, J. A., Candela, S.A., Ríos, C. A., Montes, C., and Uribe, C., 2009, Spontaneous combustion of the Upper Paleocene Carrejón Formation coal and generation of clinker in La Guajira Peninsula (Caribbean Region of Columbia); International Journal of Coal Geology, v. 80, p. 196–210.

Ross, M., and Huebner, S., 1979, Temperature-composition relationships between naturally occurring augite, pigeonite, and orthopyroxene at one bar pressure: American Mineralogist, v. 64, p. 1133–1155.

Smith, K., 2007, Strategies to predict metal mobility in surficial mining deposits: Reviews in Engineering Geology, v. 17, p. 25–45.

Soco, E., and Kalembkiewicz, J., 2007, Investigations of sequential leaching behavior of Cu and Zn from coal fly ash and their mobility in environmental conditions: Journal of Hazardous Materials, v. 145, p. 482–487.

Spieker, E. M., 1931, The Wasatch Plateau Coal Field, UT: United States Geological Survey, Bulletin 819.

Stracher, G. B., Tabet, D. E., Anderson, P. B., and Pone, J. D. N., 2005, Utah's state rock and the Emery coal field: Geology, mining history, and natural burning coal beds: Geological Society of America Field Guide 6, p. 199–210.

Stracher, G. B., and Taylor, T., 2004, Coal fires burning out of control around the world: thermodynamic recipe for environmental catastrophe: International Journal of Coal Geology, v. 59, p. 7–17.

Sujanti, W., and Zhang, D., 1999, A laboratory study of spontaneous combustion of coal: the influence of inorganic matter and reactor size: Fuel, v. 78, p. 549–556.

Tilley, C., 1924, Contact metamorphism in the Comrie area of the Perthshire Highland: Quarterly Journal of the Geological Society of London, v. 80, p. 22–77.

United States Environmental Protection Agency, Drinking Water Contaminants, National Primary Drinking Water Regulations: http://water.epa.gov/drink/contaminants/index.cfm#seven (accessed November 2013).

Yudovich, Y., and Ketris, M., 2005, Mercury in coal: a review, Part 1. Geochemistry: International Journal of Coal Geology, v. 62, p. 107–134.

APPENDIX A: COMPLETE XRF DATA FROM SAN RAFAEL SWELL, UT

SAMPLE	LOC.*	SiO_2	TiO_2	Al_2O_3	Fe_2O_3	MgO	MnO	CaO	K_2O	Na_2O	P_2O_5	Zr	Zn	Y	V	U	Th	Ta	Sr	Sm	Sc	Rb	Pr	Pb	Ni	Nd	Nb	La	Hf	Ga	Cu	Cr	Ce	Ba
13UT-1	E	83.68	0.27	5.56	2.48	0.05	0.00	0.21	1.47	0.54	0.06	315.70	38.20	20.90	15.80	bdl	6.30	6.10	39.20	bdl	7.40	48.80	4.90	12.00	10.40	bdl	9.10	13.20	6.50	5.60	bdl	20.30	bdl	279.10
13UT-4	E	82.51	0.09	5.44	2.28	0.04	0.00	0.60	1.10	0.52	0.05	63.70	7.00	11.50	15.30	bdl	6.00	7.80	69.10	4.20	bdl	43.40	9.80	9.00	bdl	20.60	3.20	21.30	2.10	6.40	12.50	15.10	bdl	512.80
13UT-5	EC	74.13	0.61	11.51	1.32	0.84	0.01	1.20	2.20	0.11	0.32	295.40	73.40	33.60	66.10	3.50	10.00	bdl	241.30	6.70	7.80	96.00	9.60	31.00	37.10	33.20	13.70	36.80	6.40	13.20	15.30	106.10	bdl	428.30
13UT-6	EC	72.13	0.64	12.79	0.87	0.72	0.00	0.45	2.20	0.09	0.11	283.30	52.60	20.10	84.90	2.80	7.80	3.40	388.60	6.50	8.60	98.90	7.00	6.60	22.00	5.70	13.60	30.00	5.70	15.80	17.30	112.40	56.60	387.50
13UT-7	EC	79.68	0.55	9.14	1.11	0.65	0.02	0.94	1.87	0.05	0.22	402.80	35.50	23.40	41.60	2.20	7.80	8.00	118.50	4.20	3.70	71.80	4.70	8.90	22.70	23.80	12.10	30.60	7.70	11.10	5.80	59.90	59.70	263.20
13UT-8	EC	81.34	0.33	4.97	1.03	0.63	0.02	1.72	0.99	0.11	0.20	330.30	35.70	19.80	26.50	3.40	7.60	bdl	64.20	bdl	6.60	38.80	6.50	6.60	9.40	bdl	8.40	16.20	6.40	5.50	2.90	52.60	bdl	338.40
13UT-9	EC	76.24	0.16	2.60	1.05	0.78	0.03	6.83	0.60	0.03	0.12	194.90	23.60	13.40	15.70	bdl	4.60	bdl	76.10	5.10	5.70	23.00	2.00	4.90	4.50	17.30	4.60	15.10	4.10	2.90	bdl	22.40	bdl	109.10
13UT-10	EC	58.69	0.48	8.61	19.19	1.57	0.38	1.43	1.47	0.02	0.30	230.50	61.00	48.20	74.50	5.10	11.50	bdl	132.10	bdl	15.70	48.90	9.40	13.40	37.60	41.50	10.40	40.30	4.60	10.30	14.50	68.10	69.50	274.70
13UT-12	EC	79.19	0.49	7.85	0.98	0.60	0.02	1.00	1.63	0.05	0.20	421.00	33.60	23.40	38.50	2.50	8.70	5.40	109.20	6.80	6.10	62.30	6.50	10.50	14.20	22.10	12.10	21.50	8.30	8.50	4.30	50.20	bdl	262.40
13UT-15	EC	68.26	0.10	1.15	1.34	1.72	0.05	11.40	0.30	0.00	0.09	191.40	bdl	10.10	9.80	2.60	3.60	bdl	60.80	6.90	10.00	14.70	3.60	7.40	3.90	bdl	2.80	bdl	3.60	1.40	bdl	17.00	bdl	58.50
13UT-16	EC	38.12	0.03	0.41	1.87	7.91	0.03	21.31	0.13	-0.03	0.04	39.40	5.20	8.10	bdl	bdl	3.80	bdl	38.00	bdl	21.60	11.80	1.70	2.80	bdl	bdl	2.30	bdl	bdl	1.10	bdl	10.40	27.60	18.10
13UT-17	H	56.04	0.11	1.94	3.42	8.38	0.07	19.72	0.59	-0.02	0.10	127.30	35.10	7.10	10.60	bdl	4.70	bdl	62.70	bdl	17.60	17.00	3.70	16.90	bdl	bdl	4.50	8.80	3.50	2.70	10.30	19.50	51.90	303.70
13UT-18A	H	41.71	0.15	2.69	2.93	6.82	0.06	16.35	0.71	-0.01	0.10	114.20	7.40	17.00	24.60	3.10	9.60	bdl	91.50	bdl	15.70	50.00	3.60	7.30	3.20	bdl	6.00	6.80	3.70	3.00	bdl	23.70	41.70	120.40
13UT-19	H	51.04	0.46	8.86	1.80	6.26	0.06	19.16	2.00	0.06	0.24	176.50	57.50	22.00	55.50	3.10	8.60	4.50	156.60	5.10	20.60	70.80	9.10	4.60	22.60	24.80	10.00	24.40	4.10	9.90	21.60	64.40	43.30	220.90
13UT-20V	H	64.94	0.69	15.50	1.51	1.87	0.01	4.26	3.09	0.12	0.35	147.30	94.50	33.50	102.50	6.20	15.20	5.30	138.90	5.90	13.20	116.90	12.90	19.60	44.60	33.90	13.70	34.80	4.10	20.90	22.80	142.80	78.20	353.50
13-UT-21A	H	60.53	0.60	11.55	2.98	4.35	0.08	13.65	2.32	0.12	0.33	220.30	92.00	27.90	76.20	4.00	9.00	bdl	152.60	6.40	20.70	83.90	8.90	9.00	29.50	23.00	11.90	38.70	4.40	12.30	48.30	89.10	11.40	284.80
13-UT-21A	H	60.53	0.60	11.55	2.98	4.35	0.08	13.65	2.32	0.12	0.33	220.30	92.00	27.90	76.20	4.00	9.00	bdl	152.60	6.40	20.70	83.90	8.90	9.00	29.50	23.00	11.90	38.70	4.40	12.30	48.30	89.10	11.40	284.80
13UT-21A.2	H	60.32	0.59	11.44	2.96	4.03	0.07	12.70	2.33	0.06	0.32	221.90	85.80	28.20	73.40	2.90	10.70	bdl	145.90	4.20	17.50	84.80	9.30	36.10	28.00	34.70	13.40	34.60	5.50	13.10	19.10	88.40	31.40	283.90
13-UT-21B	H	51.85	0.48	8.74	4.14	7.59	0.09	21.87	1.82	0.07	0.27	195.70	60.20	23.90	59.50	bdl	10.50	bdl	154.60	bdl	25.40	62.90	7.70	6.40	30.90	23.10	11.60	27.10	4.50	10.00	13.40	66.20	98.30	231.50
13-UT-21C	H	60.25	0.59	11.20	3.55	4.35	0.08	13.85	2.22	0.08	0.32	223.30	145.80	28.90	73.60	2.10	8.30	bdl	151.30	7.10	21.80	78.00	5.40	9.50	43.30	16.90	12.00	39.00	4.70	14.90	27.00	82.20	18.10	262.80
13-UT-21E	H	59.71	0.58	11.47	2.50	4.44	0.06	13.44	2.58	0.13	0.29	183.20	95.00	30.40	74.40	5.50	10.20	bdl	160.40	6.40	16.80	89.60	7.10	21.50	42.00	31.00	10.90	32.50	3.30	12.90	16.20	97.30	bdl	353.50
13UT-21F	H	82.61	0.44	6.86	0.35	0.39	0.00	0.01	0.88	0.03	0.02	283.90	20.60	18.60	30.80	4.00	9.60	4.70	34.20	4.70	7.50	42.60	5.00	2.50	4.60	bdl	10.90	17.00	5.80	7.00	bdl	39.00	bdl	163.30
13-UT-21G	H	47.60	0.44	8.65	2.81	8.82	0.09	25.98	1.87	0.05	0.25	154.00	96.30	22.90	62.70	2.80	9.70	bdl	173.00	4.70	25.40	63.70	7.80	bdl	18.40	24.20	10.50	31.80	4.00	9.30	16.20	66.50	35.20	201.70
13-UT-21I	H	59.68	0.59	11.52	3.17	4.24	0.08	13.34	2.26	0.12	0.32	217.10	80.10	28.90	82.00	3.60	11.70	bdl	149.60	5.70	17.10	82.90	3.50	5.40	30.00	27.40	13.00	23.20	5.20	12.30	32.10	86.80	22.70	280.20

*****Location abbreviated to Loc. Location abbreviations: E – Emery, UT; EC – East Carbon, UT; H – Helper, UT.

All oxides in weight percent; all other elements in parts per million (ppm).

APPENDIX A: COMPLETE XRF DATA FROM SAN RAFAEL SWELL, UT (Continued)

SAMPLE	LOC.*	SiO_2	TiO_2	Al_2O_3	Fe_2O_3	MgO	MnO	CaO	K_2O	Na_2O	P_2O_5	Zr	Zn	Y	V	U	Th	Ta	Sr	Sm	Sc	Rb	Pr	Pb	Ni	Nd	Nb	La	Hf	Ga	Cu	Cr	Ce	Ba
13-UT-22B	H	56.75	0.48	8.84	2.22	7.21	0.06	18.67	1.90	0.05	0.25	216.50	67.30	23.10	56.00	4.60	9.50	bdl	163.90	5.90	23.80	63.10	8.00	5.80	27.90	24.50	9.80	33.90	4.50	10.80	23.70	69.70	56.80	252.10
13-UT-22D	H	50.34	0.43	8.28	2.07	9.54	0.06	25.04	1.62	0.06	0.23	198.90	98.30	20.30	57.70	4.30	7.30	bdl	196.50	bdl	27.30	54.50	6.50	7.50	25.20	26.10	8.70	32.80	3.90	9.50	12.90	56.50	72.20	645.40
13-UT-22E	H	56.70	0.47	8.57	2.12	7.72	0.06	19.53	1.82	0.04	0.25	220.30	81.30	20.90	56.70	2.40	7.20	bdl	167.50	bdl	21.00	60.40	6.40	7.50	24.90	15.10	10.00	35.20	4.40	11.60	22.20	77.50	14.80	269.50
13UT-23B	H	74.59	0.07	1.62	2.25	1.32	0.07	7.62	0.28	0.02	0.19	66.20	19.90	12.70	11.30	2.10	4.10	bdl	39.00	bdl	9.20	12.80	2.20	12.70	13.60	bdl	1.90	7.20	bdl	1.70	bdl	22.60	bdl	52.80
13UT-23C	H	71.34	0.06	1.51	2.30	1.61	0.08	8.28	0.34	0.06	0.19	60.60	24.80	13.30	12.70	bdl	3.80	bdl	44.00	bdl	5.90	15.30	3.50	14.50	12.90	bdl	2.30	11.10	bdl	2.30	bdl	20.50	bdl	59.80
13UT-24A	E	80.57	0.26	4.96	1.69	1.15	0.02	1.81	1.24	0.46	0.08	350.60	20.00	18.80	23.20	2.30	6.90	bdl	60.60	4.10	6.50	47.30	6.80	9.10	4.40	14.80	7.90	17.40	6.70	5.30	bdl	19.30	bdl	271.20
13UT-24C	E	58.94	0.99	23.86	5.64	1.01	0.06	1.37	0.82	0.14	0.04	190.10	32.20	43.80	131.70	17.50	24.50	7.50	363.50	5.70	15.20	54.70	10.60	bdl	30.00	27.20	21.20	35.60	4.00	53.70	30.20	112.10	56.40	459.30
13UT-25	E	47.57	0.50	9.65	6.70	7.68	0.14	19.55	2.37	0.08	0.27	161.10	64.10	24.00	68.30	6.60	12.50	7.10	144.60	4.30	20.50	81.70	6.80	14.90	22.30	39.50	10.90	27.20	3.90	12.00	16.00	72.30	110.30	224.40
13UT-27	E	71.12	0.21	7.66	10.21	0.10	0.00	0.19	2.06	0.60	0.13	119.20	69.20	14.10	24.50	4.90	10.40	4.50	69.90	4.60	5.50	71.80	5.20	8.60	31.30	23.10	6.70	14.00	2.80	7.70	bdl	50.40	85.30	395.70
13UT-28A	E	82.97	0.16	6.76	1.00	0.06	0.00	0.07	2.27	0.60	0.03	206.40	12.50	18.00	18.90	2.40	8.30	4.70	88.50	5.40	bdl	81.00	7.80	10.60	2.80	18.00	6.60	22.70	4.70	7.90	bdl	14.10	bdl	443.90
13UT-28B	E	81.13	0.39	5.65	2.93	0.27	0.06	0.19	0.94	0.03	0.09	430.50	265.70	44.80	26.80	2.30	9.90	5.10	44.40	4.80	7.30	37.70	5.80	10.60	32.40	18.00	10.90	15.90	8.70	5.60	13.00	36.60	bdl	144.30
13UT-28C	E	82.16	0.22	7.01	1.02	0.16	0.04	0.39	1.76	0.59	0.05	218.70	20.30	19.50	18.40	bdl	8.20	4.90	75.70	4.20	bdl	66.00	6.00	10.30	3.50	23.00	8.00	27.20	5.10	8.40	8.30	16.40	bdl	372.90
13UT-28E	E	86.15	0.21	4.32	0.22	0.08	0.00	0.38	1.08	0.32	0.02	324.60	bdl	16.40	13.80	2.30	6.90	5.30	47.10	bdl	bdl	42.70	3.60	7.10	bdl	bdl	7.30	16.10	6.40	5.90	bdl	14.30	bdl	249.70
13UT-29	E	85.91	0.23	4.00	0.89	0.28	0.00	0.49	1.17	0.45	0.02	212.60	36.40	17.00	12.10	bdl	4.10	5.20	55.20	6.50	bdl	44.20	5.30	25.30	bdl	bdl	6.30	18.10	4.20	4.00	bdl	14.70	bdl	233.10
13UT-30A	E	79.91	0.18	6.74	0.81	0.92	0.01	0.49	1.09	0.72	0.04	82.70	18.50	16.60	15.90	bdl	8.40	7.10	101.70	6.80	bdl	45.70	7.90	6.80	3.60	24.50	6.80	25.50	3.10	6.30	bdl	17.10	bdl	464.00
13UT-30B	E	80.68	0.14	3.55	1.40	0.96	0.01	2.73	0.44	0.17	0.04	110.10	24.00	15.10	17.00	2.90	4.90	5.50	58.10	7.10	8.30	22.20	7.50	2.40	12.20	9.30	3.10	15.70	2.50	4.60	1.30	2.00	32.10	173.60

*****Location abbreviated to Loc. Location abbreviations: E – Emery, UT; EC – East Carbon, UT; H – Helper, UT.

All oxides in weight percent; all other elements in parts per million (ppm).